UPPSALA UNIVERSITY & UTRECHT UNIVERSITY

MASTER THESIS CLIMATE PHYSICS

Modelling a Perennial Firn Aquifer using MODFLOW 6

A case study on the Lomonosovfonna ice cap

Authors:
Tim VAN DEN AKKER

Supervisors:
Dr. Ward VAN PELT (Uppsala Univeristy)
Dr. Carleen REIJMER (Utrecht University)

July 23, 2020

UPPSALA UNIVERSITET

Universiteit Utrecht

0

CONTENTS

0 LIST OF FIGURES

LIST OF TABLES

Abstract

Perennial Firn Aquifers (PFA's) are bodies of fresh water stored in pore spaces in firn (granular snow) for multiple consecutive years on glaciers and ice caps. PFA's can can delay glacier discharge into the ocean, affect sliding processes of glaciers and contain microbiological life. There are indications that PFA's are forming in places formerly thought to have unsuitable formation conditions, the abundance of PFA's is expected to increase in a future warming climate. The dynamic characteristics of PFA's, such as flow rates, water table depth variations and the reaction to a changing climate, are poorly understood. To date, a model of lateral flow of water in firn in general is not available. In this study, a 3D flow model of a PFA is created using the USGS modular hydrological model (MODFLOW 6) and FloPy. The area that is modelled is a grid of about 10 x 7 km on top of the Lomonosovfonna ice cap on Svalbard. The hydraulic conductivity is calibrated against field data of water table depth extracted from ground-penetrating radar data collected in 2017. It is found in this study that for a third order polynomial hydraulic conductivity as function of the density, the RMSE between model output and observations is lowest. The model was then run from 1957 to 2019, and for two RCP scenarios (RCP 4.5 and RCP 8.5) from 2019 - 2060. Our results suggest that the aquifer has been present since at least 1957 and increased in volume up to present day. The model predicts a rise in the water table in both future scenarios, more pronounced in the RCP 8.5 scenario. The modelled water table reaches the surface around 2044 (RCP 8.5) and 2048 (RCP 4.5), more cells will eventually have a water table at the surface in the RCP 8.5 scenario compared to the RCP 4.5 scenario. Future research can use this model as a starting point to model more elaborate firn-PFA interactions, such as freezing of the water table. Also, more research can be done to develop an above-surface routine for the water, such as runoff or lake formation. The density-dependent hydraulic conductivity can be used on other glaciers or ice caps to perform similar model experiments.

Plain language abstract

Liquid water storage in snow, referred to as firn aquifers, is believed to be more common in a warming climate. Liquid water storage in snow can slow down sea level rise, accelerate sliding of glaciers and contain micro-organisms such as bacteria. In this research, a model of liquid water storage and movement in snow layers is presented. The resistance of snow to water flow is not yet know, and is used to tune the model in this research to get as close to observed water depths as possible. The optimized model is then run from 1957 - 2019 to study the formation of the firn aquifer. Then, the model was run for two future scenarios from 2019 - 2060: one with medium climate change, one with strong climate change. The aquifer studied in this research was likely already present before 1957. In both future scenarios, the water will get closer to the surface of the ice cap and will eventually reach it around 2045, a little sooner for the strong climate change scenario, and a little later for the medium climate change scenario. Water flow magnitudes will increase, and as a consequence the residence time of water in the glacier will decrease.

The image used in the heading shows Prof. Veijo Pohjola, conducting mass-balance measurements on the Lomonosovfonna ice cap during a field campaign in 2009

By 2100, the mean sea level is predicted to have increased with 0.44 meter (0.29 - 0.59 m, *likely* range) in the least-emission RCP scenario (RCP 2.6), and with 0.84 (0.61 - 1.10 m, *likely* range) in the Business as Usual scenario (RCP 8.5), compared to the mean of 1986 - 2005 (Oppenheimer et al., 2019). Glaciers, the Antartic Ice sheet and the Greenland Ice Sheet (GrIS) are respectively the second, third, and fourth highest contributors to sea level rise, after thermal expansion (Church et al., 2013). One of the uncertainties in predicting the contributions to sea level rise from the above mentioned sources is runoff interception by multi-year water storage in firn layers, referred to as Perennial Firn Aquifers (PFA's) (Church et al., 2013).

Aquifers, defined in groundwater analysis as an underground layer of permeable material that trap liquids in its pore space, can hold substantial volumes of water. In groundwater problems, the permeable material can for example be sand, rocks and/or clay. Firn, defined as multi-year snow with a lower density than ice, contains pore spaces and can therefore contain water, equivalent to sand, rock or clay in a groundwater aquifer system. Kuipers-Munneke et al. (2014) found that aquifers can form in firn layers of ice caps and glaciers, if certain meteorological conditions are favourable. Forster et al. (2014) found a firn aquifer that persisted for multiple years of roughly 70,000 km^2 in southeastern Greenland in 2014 using airborne radar data. The water storage capacity of this PFA is calculated to be roughly equivalent to 0,4 mm of eustatic sea level rise (Koenig et al., 2014).

Water flow in PFA's is driven by hydraulic head gradients and disappears as a result of several processes. Water input to a PFA can for example be surface meltwater or rain. Poinar et al. (2017) pointed out in a model study that water flows from the aquifer enhanced the formation of deeper crevasses, which eventually hydrofracture through the bed. Running the same model without the PFA caused the meltwater to refreeze without reaching the bed (Poinar et al., 2017). Recently, surface melt water streams have been identified on Antarctica that are said to be able to form firn aquifers (Kingslake et al., 2017). Radar observations of an East Antarctic outlet glacier indicate the possible presence of a PFA, comparable to the one found on the GrIS (Schaap et al., 2019, Lenaerts et al., 2017, Lenaerts et al., 2018). Fountain (1989) found liquid water stored in the firn of the South Cascade Glacier, Washington State, USA. For three consecutive summers, there was water present, suggesting the presence of a PFA. PFAs were also discovered on the Svalbard archipelago, for example on the Holtedahlfonna (Christianson et al., 2015), and on the Lomonosovfonna (Hawrylak and Nilsson, 2019).

Koenig et al. (2014) suggest that firn aquifers buffer sea level rise, because they delay fresh water runoff. However, the firn layers latent heat content increases as water percolates and refreezes. This effectively warms the firn layers and slows the cooling of the firn in the cold season (Kuipers-Munneke et al., 2014), thereby decreasing the cold content of the firn. A lower cold content means that the firn will heat up quicker and (partly) melt, making it more sensitive to an increasing surface temperature. This is confirmed by Kuipers-Munneke et al. (2015), but the sensitivity to an increased surface temperature is found to vary strongly with the accumulation rate. Also, recently Miller et al. (2020) found that the residence time of water in a firn aquifer is approximately 6.5 years, suggesting that pore space only act as a short term storage and not as a buffer to sea level rise.

If water at the surface of an ice field does not percolate into the firn, but stays at the surface, supraglacial lakes and streams may be formed. These supraglacial lakes and streams have in general a lower albedo compared with the surrounding snow, making them warm quicker (Kuipers-Munneke et al., 2014). As the water passes through dry firn pore spaces towards the top of the PFA, small portions of the water will remain in the pore spaces due to capillary forces.

This remaining water is referred to as irreducible water. The remaining percolating water will raise the standing water column and become part of the PFA.

Firn aquifers have caught attention in the field of microbiology. Recently, studies were done to assess microbiological life in firn aquifers, and it is found that algae, bacteria, and viruses can persists in aquifers (Boetius et al., 2015), and grow in number with an order of 4 every year they persist (Christner et al., 2018). If the aquifer is close enough to the surface, where porous snow does not fully block sunlight, whole ecosystems could develop (Stevens et al., 2018). Microbiological life was detected at the snow-bedrock interface in Ny-Ålesund, Svalbard, in 2010 by Larose et al. (2010). It is further argued by Gallet et al. (2019) that microbiological life in snow layers could affect the chemical composition of snow, and change the surface albedo, thereby changing glacier melt rates.

Efforts have been made to model the formation of firn aquifers. Kuipers-Munneke et al. (2014) present a one dimensional aquifer model, which is designed to asses under what climatic conditions an aquifer will form, and how wet firn responds to climate change, compared to dry firn (Kuipers-Munneke et al., 2015). Efforts have also been made to asses the capability of different models to predict vertical meltwater percolation (Steger et al., 2017,Marchenko et al., 2017b). Most of those models were originally developed for avalanche predictions (Bartelt and Lehning, 2002). Vertical percolation and refreezing is more elaborately solved in the 1D Crocus/SURFEX model (Vionnet et al., 2012), and also the Richardson Equation is used to model vertical water flow (Wever et al., 2014). However, these studies do not include lateral movement of water in the firn aquifer.

The main focus of this thesis is the development of a 3D water movement model of a PFA, tuned to observations by varying the hydraulic conductivity. The model makes it possible to simulate the evolution of the water table height over the past and into the future, therefore showing the temporal evolution of the aquifer. The model gives insights on the distribution of the hydraulic conductivity of firn snow, and increases understanding of the dynamics of a PFA, water movement speed, lifetime of water in an aquifer and the reaction of a PFA to changing climatic conditions. The PFA model is used to simulate the historical development of the aquifer from 1957 to 2019, and forced with two future scenario data sets, that contain data for the period 2019 - 2060, to asses the response of the aquifer to a changing future climate (RCP 4.5 and RCP 8.5). The area of study is the Lomonosovfonna ice cap on central Spitsbergen, the largest island of the Svalbard-archipelago. Data on water table height is available. In addition, there is modelled density, depth and runoff data available for the ice cap, obtained from an Energy Balance Firn Model (van Pelt et al., 2012, van Pelt et al., 2019). In this thesis, an existing groundwater flow simulator called MODFLOW 6 (Langevin et al., 2017), is used to model the PFA on the Lomonosovfonna ice field. MODFLOW 6 is the latest hydrological model developed by the USGS, widely used to simulate groundwater flow.

This thesis is structured as follows: in chapter 2 the theories of fresh water storage in firn layers and general groundwater flow are discussed. In chapter 3 the study area is presented. Chapter 4 deals with the model developed in this study, and what input data is used and how this is processed. In chapter 5, the results of the tuning process are presented. In chapter 6, the results of the three model experiments are shown. Chapter 7 consists of a discussion of the results presented in chapter 6, and lists the limitations of this study. Chapter 8 contains the final conclusion of this study.

2

In this chapter, the theory of groundwater flow and water storage in firn layers is described. First, in sections 2.1 and 2.2, the theory on water storage in firn layers, and the effect of the stored water on the firn conditions, is discussed. Then, in section 2.3, the general governing equation for groundwater flow, Darcy's law, is described. To conclude, in section 2.4 typical aquifer properties are explained.

2.1 Fresh water storage in snow layers

The dominant parameter determining the water storage in firn is the pore volume. The expression for the pore volume as a percentage of the total volume in a sample of firn snow, referred to as the porosity of the firn, is presented in Eq. 2.1, in which ρ is the density of the firn snow sample, ρ_i the density of ice (typically 920 kg m$^-$3) and P the porosity.

$$P = 1 - \frac{\rho}{\rho_i} \tag{2.1}$$

Porosity is unitless and can be interpreted as the percentage of the volume of a sample that is not filled with the bulk medium. Often, pore spaces are filled with air, and can become filled with a percolating liquid. This can happen in firn layers, by for example percolating surface melt or rain.

The second way water can be stored in the firn pack is referred to as the irreducible water content, which is the water stored in the pore spaces of firn by adhesive and capillary forces. Irreducible water content (W_c) is related to the porosity according to Eq. 2.2 and is expressed as the mass ratio of the irreducable water and the mass of the layer (Reijmer and Hock, 2008). For low density firn, for example 350 kg/m^3, using Eq. 2.1 and Eq. 2.2, this would give an irreducible water content expressed as the fraction of the total mass of a firn layer of roughly 0.08. For a box of 1 m^3 of firn (350 kg with the given density) this would mean that there is, after gravity drainage, roughly 28 kg of water left in the pore spaces. This amount decreases as the density increases.

$$W_c = 0.0143e^{3.3P} \tag{2.2}$$

Percolating water from the surface undergoes a few processes before reaching the PFA and becoming 'stored water'. Consider a volume of water entering the top of the firn column. First, it will refreeze until the firn becomes temperate. Then, a small amount of water will stay in the firn as irreducible water content. The remaining water will percolate further in the firn and the same processes happen again until the water encounters a impermeable layer, which can be ice or bedrock. Then, the water starts to pile up from this impermeable layer up, saturating pore spaces, to create a standing water column, referred to as the PFA. The top of this water column is referred to as the water table. The water can then move horizontally, following the gradient in water tables.

As shown by Kuipers-Munneke et al. (2015), certain meteorological conditions favor the formation of a PFA, their model study showed that a high accumulation rate is needed to provide enough pore space and insulation for the aquifer to persists, in combination with a high surface melt rate to provide enough input water.

2.2 Effect of water on thermodynamics

Water in the PFA influences the thermodynamics of a firn layer. The specific heat capacity of water is twice as high compared to the one of firn (4.168 J/g*K and 2.1 J/g*K respectively). This implies that, if the water temperature, T_{water}, lowers with a certain temperature difference, ΔT, it will raise the temperature of the surrounding firn, T_{firn}, with almost $2\Delta T$ (if the mass of the water and the surrounding firn are equal). If T_{water} reaches the freezing point T_{freeze}, and T_{firn} is lower than T_{freeze}, then the water will (re)freeze and the latent heat content of the water increases T_{firn}.

Refreezing of meltwater that percolates into the firn buffers some of the mass loss of glaciers, as the water refreezes and becomes part of the snowpack again (van Pelt et al., 2016b). It has been found by van Pelt et al. (2016b) in a model study of an idealized glacier that refreezing results in firn heating and densification. Although refreezing slows down mass loss, the effect on the total mass balance is much smaller than the net refreezing rate (van Pelt et al., 2016b). This suggests that melt-enhancement effects after refreezing, such as higher firn temperature, counteract the mass buffering (van Pelt et al., 2016b). The buffering effect of refreezing is also found in a comparable model study on the Kongsvegen and Holtedahlfonna glacier systems (van Pelt and Kohler, 2015). van Pelt and Kohler (2015) found that there is an slightly positive area average mass balance change (0.08 m w.e a^{-1}), and that refreezing accounts for an increase in mass balance of 0.18 m w.e. a^{-1}

Other effects of aquifers in firn layers on the glacier or ice sheet are (not exhaustive) increased basal lubrication (Christianson et al., 2015), sudden drainages (Jökulhaup-like) (Koenig et al., 2014), and hydrofracturing of crevasses (Poinar et al., 2017).

2.3 Groundwater flow

Liquid flow in porous media is governed by Darcy's law, which states that a liquid will flow from areas with a higher water surface elevation (often called head height, water table or water table height, here we will use the latter) towards areas with a lower water table height. It is found experimentally by Miller et al. (2020), by using salt injection in boreholes in an aquifer on the GrIS, that water flow in a PFA generally obeys Darcy's Law and can therefore be approached as a groundwater flow system. The simplest form of the Darcy equation can be observed in Eq. 2.3, in which q is the flow per unit area [in m s^{-1}], k the hydraulic permeability [in m^2], μ the dynamic viscosity of the fluid [in Pa.s] and ∇p the pressure gradient vector [in Pa m^{-1}]. The hydraulic permeability is a measure of how easy a fluid moves through a medium. A higher k indicates less resistance from the medium to the flow. Often, hydraulic conductivity and hydraulic permeability are interchangeably used. The most important difference is that hydraulic conductivity is a property of the medium, while hydraulic permeability is a property of the flow and the medium combined. The dimensions of hydraulic conductivity are lengths per time, often meters per second, and the dimension of the hydraulic permeability is area, often expressed in square meter or Darcy (D). Hydraulic conductivity and hydraulic permeability are linked in Eq. 2.4, in which K is the hydraulic conductivity [in m s^{-1}], k the hydraulic permeability[m^2], ρ the density of the fluid [in kg m^{-3}], g the gravitational acceleration [in m s^{-2}] and μ the viscosity of the fluid [in Pa s].

$$q = -\frac{k}{\mu}\nabla p \tag{2.3}$$

$$K = \frac{k\rho g}{\mu} \tag{2.4}$$

4

It is assumed in Eq. 2.3 that the hydraulic permeability (and therefore indirectly the hydraulic conductivity) remains spatially constant, and all sources and sinks of the water are summarized in the ∇p term. A more comprehensive Darcy equation, adapted from Langevin et al. (2017), is given in Eq. 2.5.

$$\frac{\partial}{\partial x}(K_{xx}\frac{\partial h}{\partial x}) + \frac{\partial}{\partial y}(K_{yy}\frac{\partial h}{\partial y}) + \frac{\partial}{\partial z}(K_{zz}\frac{\partial h}{\partial z}) + Q'_s = SS\frac{\partial h}{\partial t} \tag{2.5}$$

Equation 2.5 is a general mass balance for water in an aquifer, in simple terms stating: 'All flows in and out a sample volume combined will give a net in- or outflow of the liquid, that changes the water storage and therefore the water table height'. Net outflow will lower the water table height and vice versa. The first three terms on the left hand side of equation 2.5 represent the flow due to differences in water table height. Q'_s represents different sources and sinks, such as surface runoff, evapotranspiration, wells and precipitation. Those sources and sinks can be spatially and time dependent. The SS term on the right hand side refers to storage, which is the water released or stored per drop of water table height. K_{xx}, K_{yy} and K_{zz} are the hydraulic conductivities that control the speed of the water flow in respectively the x, y and z direction.

Note that Eq. 2.5 can be solved directly for h, which is the water table height of the water column, whereas Eq. 2.3 can be solved for ∇p. The water table height is generally used in groundwater modelling as output, and is also the main focus in this research.

One could argue that a PFA is a multi-phase flow system, as it consists of water both in liquid and solid state. Multi-phase flow is very common in e.g. oil pumping, as often oil is both present as liquid and gas in the porous medium. Solid-liquid flow, often referred to as 'slurry flows', are flows in which particles of the solid matter flow along with the liquid. In this research, the assumption is made that the medium consists strictly of solid water, and that the flow consists strictly of liquid water, therefore making a PFA a single-phase flow system. For a comprehensive overview of the fundamentals of multi-phase flow, the reader is referred to Brennen, 2005 . More specific literature on solid-liquid flows, in particular in pipes, can be found for example in Zandi, 2013

2.4 Aquifer properties

The properties of an aquifer, following Eq. 2.5, are presented in this section, starting with the hydraulic conductivity, followed by storage and concluded by the sources and sinks of an aquifer.

2.4.1 Hydraulic conductivity

Hydraulic conductivity controls the speed of the flow through the medium, and has dimensions distance over time. There are several ways of determining the hydraulic conductivity. One can for example experimentally determine it by slug tests, where a sample of the medium is taken and a tracer fluid is injected to determine how fast the tracer moves through the medium (D. Lewis et al., 1966). Six other methods to determine the hydraulic conductivity are described and compared by Stolte et al. (1994).

The hydraulic conductivity can be determined empirically by using models, or by using empirical relations between observed porosity and conductivity (Ringrose and Bentley, 2016). An example of such an relation, adapted from Urumović and Urumović Sr (2016), is shown in Eq. 2.6 in which K_{KC} is the hydraulic conductivity [in m/s], C_{KC} is an unitless empirical constant being $\frac{1}{180}$, g the gravity acceleration [in m s^{-2}], ν the viscosity [in m^{2}s^{-1}], P the porosity and D_{10} the grain diameter for which 10% of the sample is finer. Using Eq. 2.6 to compute the hydraulic

conductivity makes it indirectly dependent on the density (through porosity and Eq. 2.1) and temperature (viscosity of the liquid is slightly dependent on the temperature).

$$K_{KC} = C_{KC} \frac{g}{\nu} \frac{P^3}{(1-P)^2} D_{10}^2 \tag{2.6}$$

Studies have been done to estimate the hydraulic conductivity of firn snow. Fountain and Walder (1998) examined field tests of five different glaciers and found a range of $1 - 5 \times 10^{-5}$ m s^{-1}. Fountain and Walder (1998) argue that firn conditions are therefore uniform between glaciers, because of the low range in measured hydraulic conductivity. Miller et al. (2017) did slug tests on the Greenland Ice Sheet (GrIS) and found hydraulic conductivities ranging between 2.5×10^{-5} m s^{-1} and 1.1×10^{-3} m s^{-1}. Stevens et al. (2018) found in their literature review a range of 10^{-6} - 10^{-2} m s^{-1}. However, using similar techniques as Miller et al. (2017) on 10 northern hemisphere glaciers (in Canada, Svalbard, northern Sweden, Greenland and the Alps), Stevens et al. (2018) found values for the hydraulic conductivity ranging between 0.003 m day^{-1} to 3.519 m day^{-1} (3.47 10^{-8} m s^{-1} - 4.07 10^{-5} m s^{-1}), which is lower than the range from their literature review and the measurements of Miller et al. (2017).

2.4.2 Storage

The SS-term in Eq. 2.5 relates to the water being released or taken up by the pore spaces in the medium if the water table respectively rises or lowers. Storage in groundwater analysis is often determined by sum of two processes: Specific Yield (S_y) and Specific Storage (S_s). Specific yield, often referred to as effective porosity, is the volume of water that an aquifer can hold per volume of porous medium. Specific Yield is therefore dimensionless. Specific Storage is the volume of water released from the aquifer per unit decline of head from viscosity and compressibility related processes (such as the expansion of the water when the water pressure decreases), and is defined by the compressibilities of the medium and the fluid. Specific storage has dimensions [L^{-1}], and is equivalent to the irreducible water content W, but not identical. The specific storage can be calculated using Eq. 2.7, in which ρ is the density of water, g the gravitational acceleration, α the compressibility of the medium, P the porosity of the medium and β the compressibilty of water. The total storage SS can be calculated using Eq. 2.8, in which b is the thickness of the aquifer.

$$S_s = \rho g(\alpha + P\beta) \tag{2.7}$$

$$SS = S_y + S_s b \tag{2.8}$$

Storage is different for unconfined and confined aquifers. An unconfined aquifer is an aquifer in which the water table is in direct contact with the air, through the medium. An confined aquifer is sealed off from the outside air by an impermeable layer. A schematic overview, taken from NGWA (2020), is presented in Figure 2.1. In an confined aquifer, gravitational drainage and therefore the specific yield is zero, making specific storage the only contributor to the total storage. In an unconfined aquifer, both specific storage and specific yield determine the storage, but $S_y >> S_s b$ for an unconfined aquifer. Characteristic values of the specific storage for different media range between 10^{-4} - 10^{-6} m^{-1}, according to Batu (1998). With an aquifer thickness around 10 meters, the specific storage term in equation 2.8 is in the order of magnitude of 10^{-5} - 10^{-3} , while the specific yield (effective porosity) is in the range 10^{-1} - 10^0, making it at least two orders of magnitude larger than the specific storage S_s. Specific storage is an input parameter for the 'STO' package in MODFLOW 6, and a value of 10^{-5} is assigned to it, being the average value found in literature. More on the MODFLOW 6 packages is presented in Chapter 4
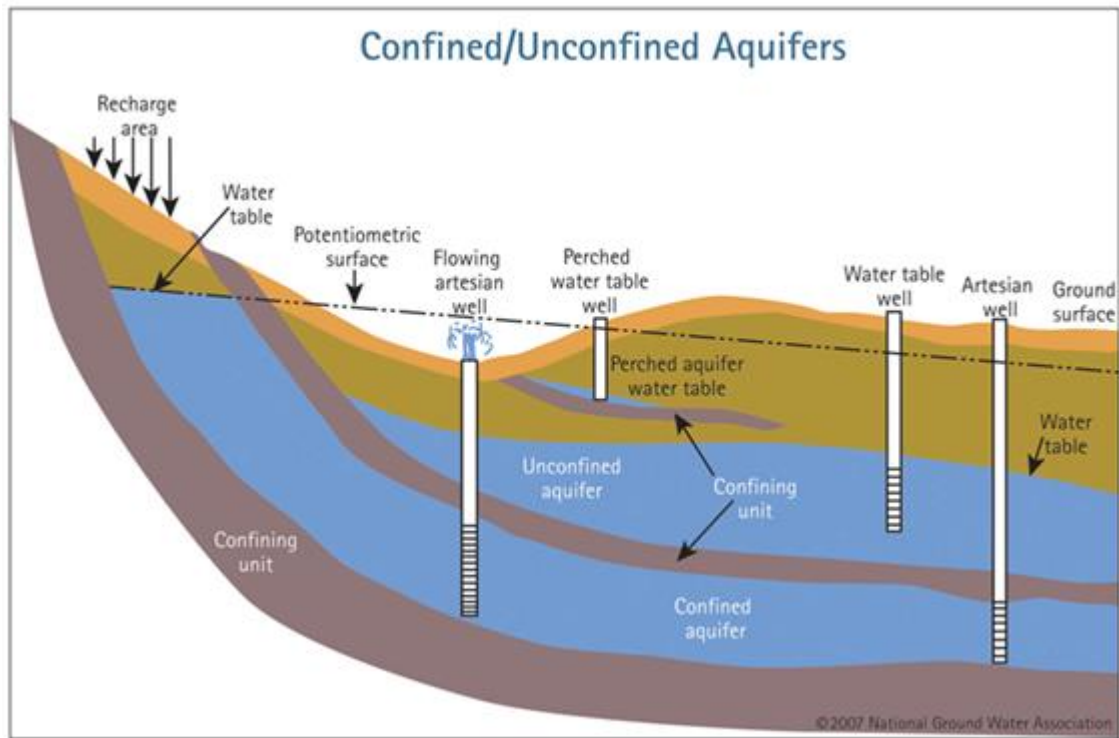
Figure 2.1: *Unconfined and confined aquifers explained, from NGWA, 2020*

2.4.3 Sources and sinks

Sources and sinks for a groundwater system are summarized in the term Q'_s in Eq. 2.5. This term includes external sources and sinks of a groundwater system. Examples include precipitation, evapotranspiration, surface streams and wells. These sources and sinks can be constant or time dependent, spatially dependent, water table height dependent or dependent on all three before mentioned factors. For firn layers, the main source is expected to be surface melt that is not refrozen or stored as irreducible water on its way down to the surface of the PFA.

Two main sinks mentioned in the literature for water in firn aquifers are crevasses and moulins (Fountain and Walder, 1998, Poinar et al., 2017, Stenborg, 1973, Everett et al., 2016, Shannon et al., 2013). The water can either be stored and transported in the crevasses, in which case the crevasse acts as a channel. Or the water can deepen it because of the pressure increase on the crevasse. The last process is referred to as hydrofracturing, and it can cause the water from the aquifer to reach the bed of the glaciers. A moulin, being a hole in the firn layer, can transport the water instantly to the bed (Catania and Neumann, 2010).

Increased surface melting is often linked to increased ice velocities and mass loss. Parizek and Alley (2004) confirm the results of Zwally et al. (2002) by using simulations that increased surface melt increases ice velocities, higher ablation rates and more mass loss, because of drainage of the surface melt to the bed of the glacier. Shannon et al. (2013) also found that there is a strong link between surface melting and ice sheet flow , and van de Wal et al. (2008) found large accelerations of the ice flow downstream of large moulins. Once the water reaches the bed of the glacier, and may form a layer between the bed and the ice, it can enhance basal sliding by a decrease in friction between the bed and the ice sheet (Hubbard et al., 1995), known as 'basal lubrication'. However, van Pelt et al. (2018) found that there is a more complicated relation between surface melt and runoff, as the amount of surface melt might change the subsurface

drainage system, and thereby change the amount and velocity of water that reaches the bed. Once a location specific surface melt threshold is reached, it is likely that the drainage system transforms from an inefficient distributed system to a channeled efficient system, decreasing the effect of surface melt on ice velocities (van Pelt et al., 2018).

The Svalbard archipelago is situated at the end of the Gulf Stream and at the Southern edge of the Artic winter sea ice cover. Because of the warming effect of the Gulf Stream, the temperature is higher than one would expect it to be given the lattitude (77°N to 80°N) (Hawrylak and Nilsson, 2019). The Svalbard climate is very sensitive to trends and variability in the sea ice cover (Divine and Dick, 2006, Day et al., 2012) and atmospheric circulation patterns (Hanssen-Bauer and Førland, 1998). Due to several feedback mechanisms summarized in the term Arctic amplification (see for example Serreze and Barry (2011)), Svalbard experiences a more rapid and amplified climate change with respect to the global mean (van Pelt et al., 2016a).

The annual average air temperature is projected to increase with 7 °C and 10 °C between the periods 1971 - 2000 and 2071 - 2100, for respectively medium and high anthropogenic CO_2 emissions (Hanssen-Bauer et al., 2019). Precipitation is expected to increase (45 % and 65 % for respectively medium and high anthropogenic CO_2 emissions), and events of heavy rainfall will grow in number and intensity (Hanssen-Bauer et al., 2019). Furthermore, the snow season is expected to shorten (Hanssen-Bauer et al., 2019).

The Lomonosovfonna ice cap is situated at the center of Spitsbergen, the largest island of the Svalbard-archipelago, see Figure 3.1. It is the highest ice cap of Svalbard (Pohjola et al., 2002), reaching up to 1250 m a.s.l on its highest point, and shaped like a gently sloping dome. The equilibrium line on one of the largest outlet glaciers, the Nordenskiölbreen, is estimated at 719 m a.s.l. (van Pelt et al., 2012). The thickness of the Lomonosovfonna ice cap is 190 m (Marchenko et al., 2017a), and it feeds into several outlet glaciers, of which the Nordenskiöldbreen, Grusdievbreen and Mittag-Lefflerbreen are the three largest (Isaksson et al., 2001). The Nordenskiölbreen and the Lomonosovfonna ice cap are monitored since 1997 by the Uppsala Univeristy and Utrecht University. The monitoring program consists of a.o. mass balance monitoring, ice velocity measurements, ice thickness measurements and weather observations. Useful data for this research from the monitoring program consists of firn conditions and observed water table depths. A map of the Lomonosovfonna, with elevation lines and the locations where the observations were done, is presented in Figure 3.1b. The surface height of the modelled grid on the Lomonosovfonna ice cap is shown in Figure 3.2.

Previous glaciological studies, using the data from the monitoring program, on Nordenskiöldbreen and the Lomonosovfonna ice cap have assessed climatic mass balance (van Pelt et al., 2012), snow and firn conditions (Marchenko et al., 2017a, Marchenko et al., 2017b, Marchenko et al., 2019, Pohjola et al., 2002, van Pelt et al., 2014, Vega et al., 2016), and ice dynamics (van Pelt et al., 2013, van Pelt et al., 2018).
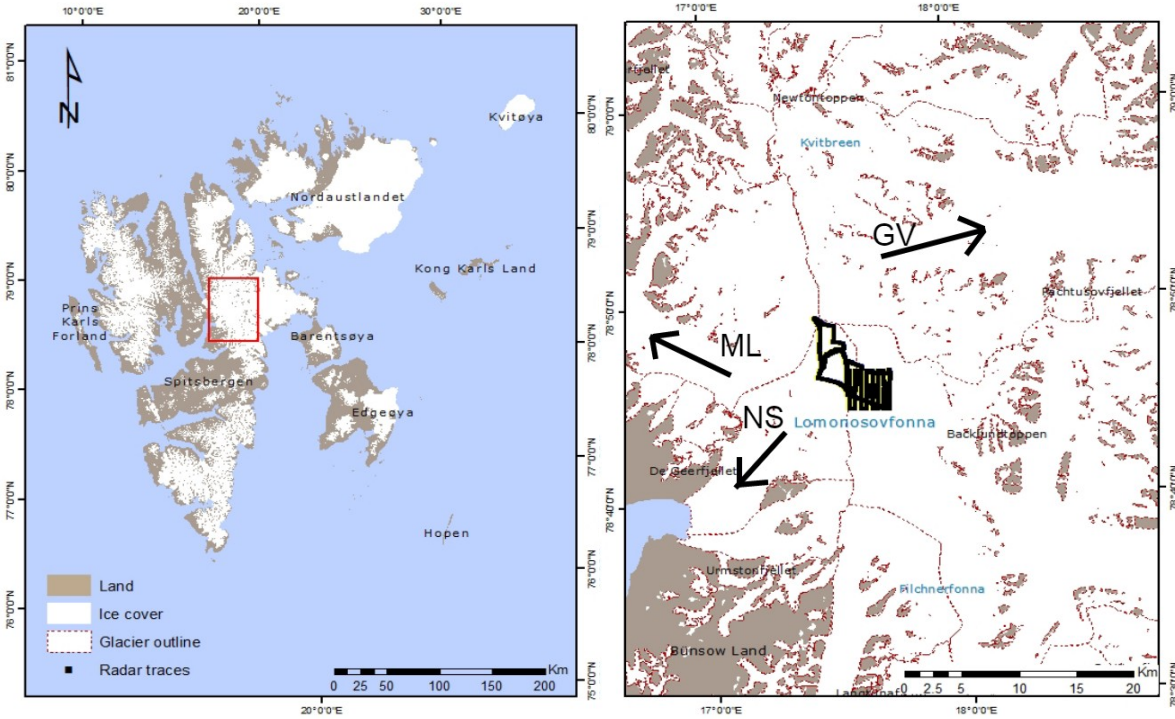
(a) *Svalbard Archipelago*

(b) *Locations of the observations*

Figure 3.1: *The Svalbard Archipelago (Figure 3.1a) and the location of Lomonosovfonna and the observations (Figure 3.1b), that have been made in 2017 in the monitoring program. Figure is adapted from Hawrylak and Nilsson (2019). NS, ML and GV refer to Nordenskölbreen, Grusdievbreen and Mittag-Lefflerbreen.*
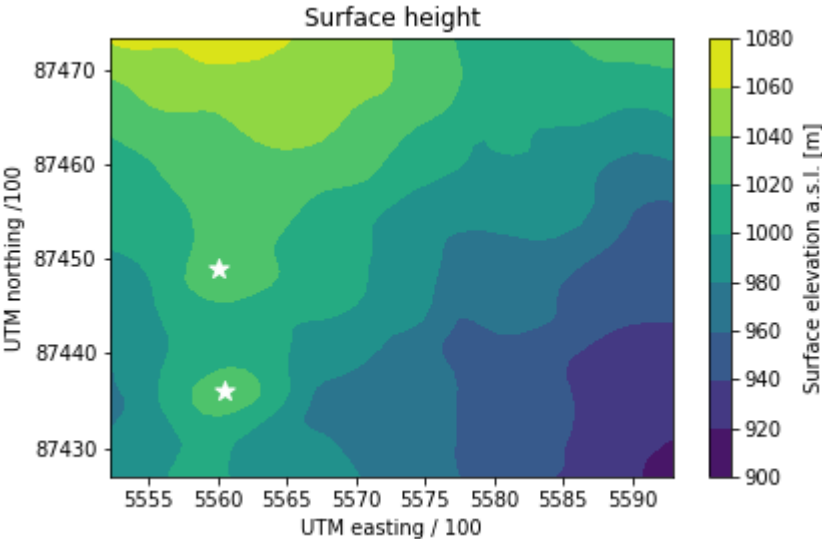

Figure 3.2: *Surface elevation profile of the model grid on the Lomonsovfonna ice cap. Two white stars indicate local peaks, that prove to be important features in the PFA modelling*

This chapter starts with an overview of the data sources and how they are processed in sections 4.1 - 4.3. Then, in section 4.4, the Lomonosovfonna Perennial Firn Aquifer Model (LPFAM) will be presented, including the numerical methods used to solve Eq. 2.5. This chapter ends with a description of the model setup and experiments presented in section 4.5 and 4.6. The area that is studied in this research is situated in the middle of the Lomonosovfonna ice cap, approximately 10 x 7 km. This area is chosen so that it contains all the observations and a bufferzone to minimize the effect of the boundary condition, this will be explained in further detail in the next chapter. The study area is discretized equidistantly in 100 rows, 100 columns horizontally and in 5 layers with increasing thickness. Time discretization is done in weeks.

4.1 Calibration data

There are water table depth observations available for the Lomonosovfonna ice cap. This data was obtained with a 500 MHz radar antenna ('Ground Penetration Radar', GPR), dragged behind a snow scooter over a grid shown in Figure 4.3, during the field campaigns in the spring of five consecutive years (2015 - 2019). The dataset of April 2017 contains the largest covered area and will be used in this research for calibration. The total length of the radar track during this field campaign is roughly 40 km.

The raw data consists of a radargram, from which the two-way travel times (twtt) of the radar signal to the reflective surface of the water table can be obtained. An example of a radargram of the observations, with a hand-picked identified water table, is presented in Figure 4.1. The twtt from the surface to the water table, identified as the red line in Figure 4.1, is then retrieved from the raw data. The twtt to the water table can be converted to a depth by using the dielectric constant of firn snow. A relation between the dielectric constant and the density of firn is given in Eq. 4.1, following Kovacs et al. (1995).

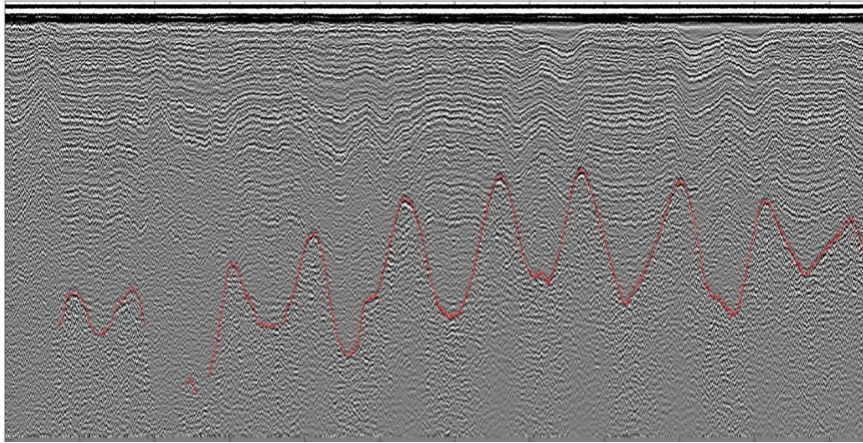**Figure 4.1:** *Example of a radargram obtained from the observations. The red line shows the presumed water table, handpicked by Hawrylak and Nilsson (2019). The figure is taken from Hawrylak and Nilsson (2019)*

$$\epsilon_f = (1 + 0.845 * \frac{\rho_f}{\rho_w})^2 \qquad (4.1)$$

Here, ϵ_f is the bulk dielectric constant of firn, ρ_f the density of the firn and ρ_w the density of water.

The velocity of the radar wave in a firn layer can then be computed using Eq. 4.2, in which c is the speed of light in vacuum and v_{int} the speed of the radar wave in the given firn layer.

$$v_{int} = \frac{c}{\sqrt{\epsilon_f}} \tag{4.2}$$

The speed of the radarwave is therefore dependent on the density of the firn. The density is obtained from an Energy Balance Firn Model (EBFM) from van Pelt et al. (2019). The EBFM will be introduced in section 4.2.2. Equations 4.2 and 4.1 are used, in combination with a depth and density profile closest to the observations, to calculate a depth-twtt profile for 75 layers ranging from the surface to ±55 meters depth. This is done by calculating the time it takes the radarwave to pass through an EBFM layer with a given density, and using the thickness of the layer to calculate per layer a depth-twtt point at the bottom of the layer. This continues for all layers. The twtt and depths are then cumulatively summed to get the total depth-twtt profile. The resulting depth-twtt plot is presented in Figure 4.2. The measured twtt is then, using linear interpolation between the closest depth-twtt points, converted to a depth of the water table. The resulting water table depth for the observations made in April 2017, plotted over the contour lines of the surface elevation of the model grid, can be observed in Figure 4.3.
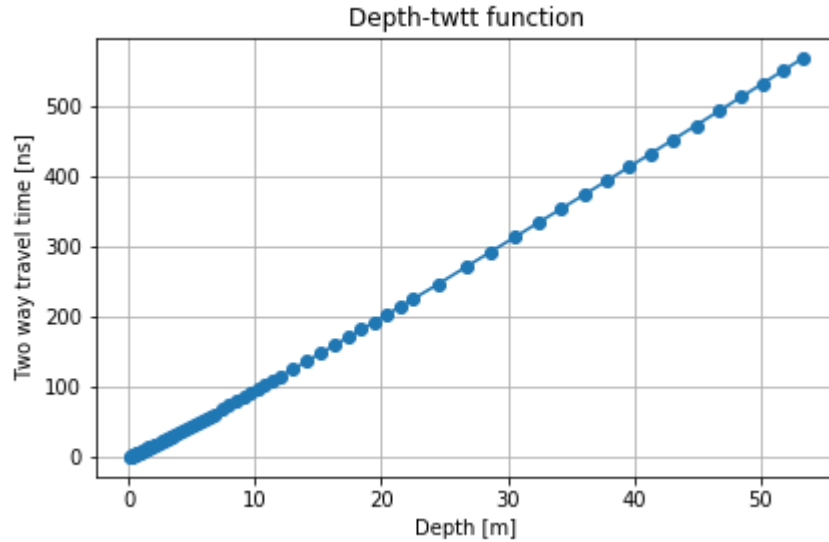
Figure 4.2: *Depth-twtt profile computed for the middle of the model grid, using a depth-density profile from the EBFM (see van Pelt et al. (2012)). Blue filled dots corresponds to calculated depth-twtt points. The observed twtt is then linearly interpolated between two calculated points to obtain the corresponding depth.*
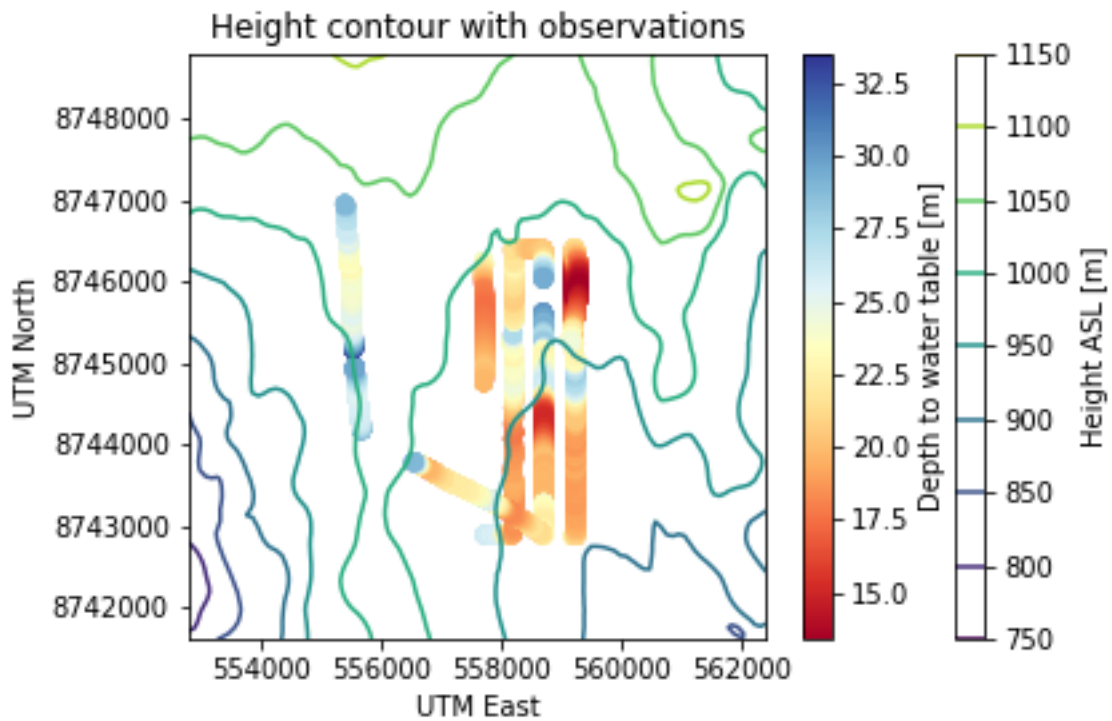
Figure 4.3: *Calculated water depths for April 2017 from GPR observations. The empty spots compared with the radartracks in Figure 3.1b have no data (i.e. 'NaN'), and were removed from the calculations. At that point, the GPR was not able to detect the water table, or the water table could not be identified from the radargram. The complete model grid is shown in this Figure. Note that the model grid is larger than the observation grid, this is done to incorporate a bufferzone to cancel out the effect of boundary conditions. This will be more elaborately discussed in chapter 5. The whole grid is situated above the equilibrium line.*

4.2 Model input data

The LPFAM uses modelled input data as surface elevation and firn conditions. A surface elevation profile of the Norwegian Polar Institute (NPI, 2014) is used to construct the top boundary of the model. A time and spatially dependent depth-density profile of the firn and time and spatially dependent meltwater input is obtained from the Energy Balance Firn Model (EBFM). The depth-density profile is used as discretization and to calculate the storage and the hydraulic conductivity per grid point in the LPFAM. The meltwater input is used as main source of water to the PFA.

4.2.1 Surface elevation data

There are two available sources of surface elevation data: 1) the DEM of the NPI (NPI, 2014) and 2) Surface altitude data from a GPS logger for the years 2015 - 2019, pulled together with the GPR over the grid shown in Figure 3.1b. To be consistent, the elevation data from 2) is used to transfer the depth of the water table observations to head heights a.s.l. , which is the common output metric of MODFLOW 6. However, the modelled grid is larger than the observations grid, as can be seen in Figure 4.3. Therefore, for model calculations and discretization, the NPI DEM will be used, because this dataset has a high resolution and is available for the whole grid, including the bufferzone. The DEM surface elevation data on the points where the observations were made did not differ significantly with surface elevation data obtained by the GPS. For all calculations done on the observed water table, such as transferring twtt to water table depth, the GPS observed surface elevation (source 2) will be used.

4.2.2 EBFM data

The most important input data for the LPFAM is the density and depth of the firn layers, and the meltwater input per grid point on the ice cap. This data is retrieved from the Energy Balance - Firn Model (EBFM) as described by van Pelt et al. (2014) and van Pelt et al. (2012) and more recently in van Pelt et al. (2019). The EBFM works as follows: first, the energy balance at the surface, presented in Eq. 4.3, is solved. Energy fluxes at the surface that are part of this model are the net shortwave radiation flux (SW_{net}), the net longwave radiation flux (LW_{net}), the turbulent heat exchange flux through latent and sensible heat (respectively Q_{lat} and Q_{sens}), the conductive heat flux into the ice (Q_{sub}) and a rain heat flux (Q_{rain}). Equation 4.3 is solved for the surface temperature with a melt energy flux (Q_{melt}) set to zero. If the resulting surface temperature is higher than 0 °C, the surface temperature is set at 0 °C and the energy fluxes in Eq. 4.3 are recomputed, but then with a non-zero melt flux Q_{melt}, which is used to compute the meltwater flux into the firn column. The EBFM requires air temperature, pressure, relative humidity, cloud cover and precipitation as input to solve the surface energy balance. The EBFM needs no input of processes that are strongly influenced by the ice surface, such as near-surface temperature, humidity and wind characteristics (van Pelt et al., 2012).

$$Q_{melt} = SW_{net} + LW_{net} + Q_{sens} + Q_{lat} + Q_{rain} + Q_{sub} \qquad (4.3)$$

Below the surface, the EBFM solves the thermodynamic equation (Eq. 4.4) and the densification equation (Eq. 4.5). The thermodynamic equation, in which ρ is the firn density, $c_p(T)$ the temperature dependent heat capacity of the firn, $\kappa(\rho)$ the density-dependent effective conductivity of the firn, F the refreezing rate, L_M the latent heat of melting ice (3.34 x 10^5 J kg^{-1}) and z the vertical coordinate (Δz is the layer thickness), describes the change of the temperature-depth profile due to heat conduction and refreezing of the meltwater resulting from the surface energy balance melt energy flux Q_{melt}. The first term on the right-hand side of Eq. 4.4 describes the vertical diffusive heat flux, the second term describes heat input from refreezing meltwater that percolates from the surface into the firn.

$$\rho c_p(T) \frac{\partial T}{\partial t} = \frac{\partial}{\partial z}(\kappa(\rho) \frac{\partial T}{\partial z}) + \frac{FL_M}{\Delta z} \qquad (4.4)$$

$$\frac{\partial \rho}{\partial t} = K_g(\rho, T) + \frac{F}{\Delta z} \qquad (4.5)$$

The densification equation (Eq. 4.5) describes the change of density of the firn due to gravitational compaction and refreezing. In Eq. 4.5, $K_g(\rho, T)$ describes density and temperature dependent compaction, F is the refreezing rate and z the vertical coordinate (Δz is the layer thickness). The minimum density in the EBFM is fixed at 350 kg m^{-3}, used for fresh snow at the surface. Gravitational compaction $K_g(\rho, T)$ is presented in Eq. 4.6, in which $C(b)$ is a accumulation dependent parameter (see Ligtenberg et al. (2011)), b the accumulation rate, ρ_{ice} the density of ice, E_c the activation energy of creep by lattice diffusion (typically 60 kJ mol^{-1}), E_g the activation energy of gain growth (typically 42.4 kJ mol $^{-1}$), R the gas constant, T the temperature of the firn and T_{avg} the temporal mean subsurface temperature (both in K).

$$K_g(\rho, T) = C(b)bg(\rho_{ice} - \rho)\exp(-\frac{E_c}{RT} + \frac{E_g}{RT_{avg}}) \qquad (4.6)$$

Water in the EBFM originates from surface melt and rain, and percolates down from the surface into the firn. First, the water refreezes when the conditions in a model layer are sufficient, being that the temperature should be below the melting point and the maximum density should be lower than the density of ice. Refreezing raises the temperature and density. If not all water could refreeze, a small portion will be stored in the layer as irreducible water content (see Eq. 2.2). The remaining water will percolate down to the next layer, where the process is repeated. This continues until the water encounters a layer that has the density of ice, where it will runoff immediately. The EBFM has a vertical extention of ±55 meter, discretized in 75 layers with increasing thickness. Horizontal water movement is not part of the EBFM.

4.3 Data processing

Most of the necessary input data is not available at the exact location of the LPFAM grid points. Therefore, the input from the EBFM and the DEM are linearly interpolated over the model grid using Python's `griddata` function. The NPI DEM has a resolution of 5 meters, the EBFM of 1 km and the LPFAM of ±100 meters. Comparisons of the resolution of the model grid with the EBFM and the DEM are presented in Figure 4.4. The DEM resolution is downgraded with a factor 5 from the original dataset of the NPI (from 1 datapoint per 5 meter to 1 datapoint per 25 meter), to make the processing more computationally efficient. This is judged as a safe method, considering that the resolution of the downscaled NPI data is still far larger than that of the model grid, as can be seen in Figure 4.4b.

The depth-density profile of the EBFM has 75 layers, the LPFAM has 5. Every 15th layer of the EBFM is therefore chosen as input for the LPFAM, so that the lowest layer in the EBFM corresponds to the lowest layer in the LPFAM. The grid averaged LPFAM density per time step, processed from the EBFM to fit the aquifer model as described before for the period 1957 - 2060, can be observed in Figures 4.5a and 4.5b. As can be seen, the average density increases in the historical period (1957-2019) (van Pelt et al., 2019) with approximately 10 kg m^{-3} over 62 years. In the RCP scenario period (2019 - 2060), the average density increases with 80 kg m^{-3} and 150 kg m^{-3} for RCP 4.5 and RCP 8.5 respectively, over 41 years.

The LPFAM grid averaged meltwater input per timestep, for the period 1957 - 2060 for both scenarios, is presented in Figures 4.6a and 4.6b. This is the meltwater that reaches the top of
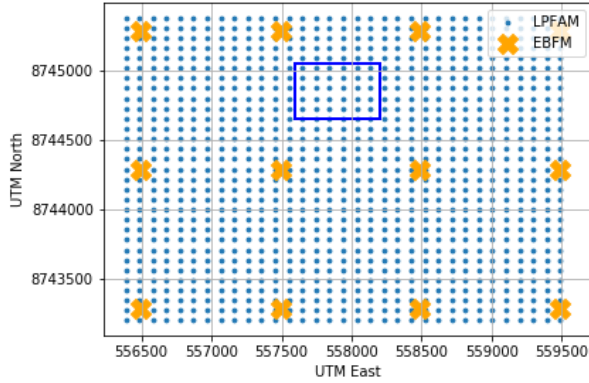
(a) *LPFAM vs EBFM*
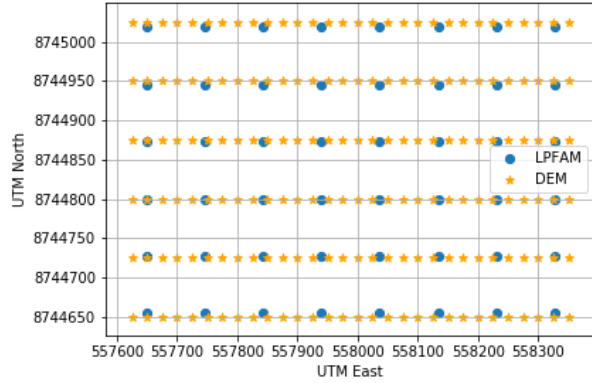
(b) *LPFAM vs DEM*

Figure 4.4: *Grid resolution of the EBFM compared with the LPFAM (Figure 4.4a) and grid resolution of the LPFAM compared with the DEM (Figure 4.4b). The blue rectangle in Figure 4.4a corresponds to the area shown in Figure 4.4b.*
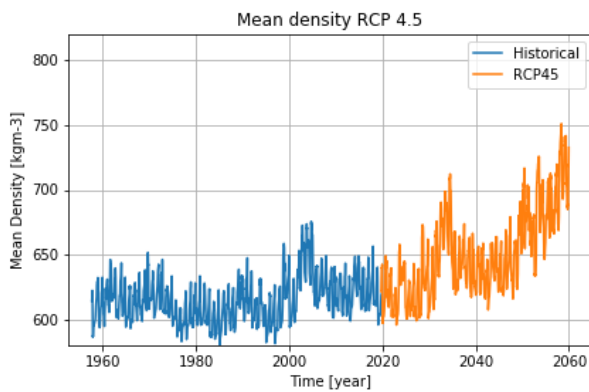
(a) *Averaged density RCP 4.5*
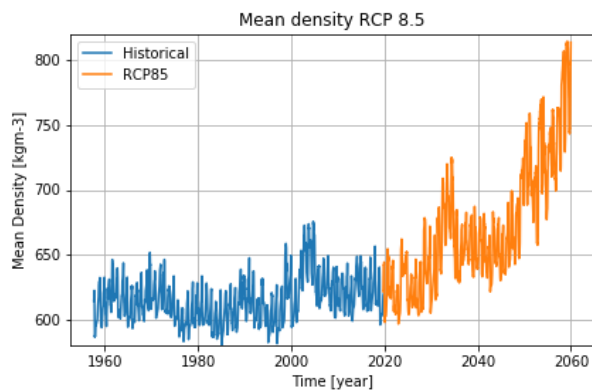
(b) *Averaged density RCP 8.5*

Figure 4.5: *Averaged density in both RCP scenarios, after the density from the EBFM was fitted to the firn aquifer model.*

the PFA in the LPFAM, but that reaches the bottom of the EBFM grid. There is a clear annual trend visible, during the melt season in the spring period, the meltwater input peaks. There is an increase in meltwater input visible over the RCP scenario period (2019 - 2060). The increase is more pronounced in the RCP 8.5 scenario compared to the RCP 4.5 scenario.

(a) *Meltwater input RCP 4.5*

(b) *Meltwater input RCP 8.5*
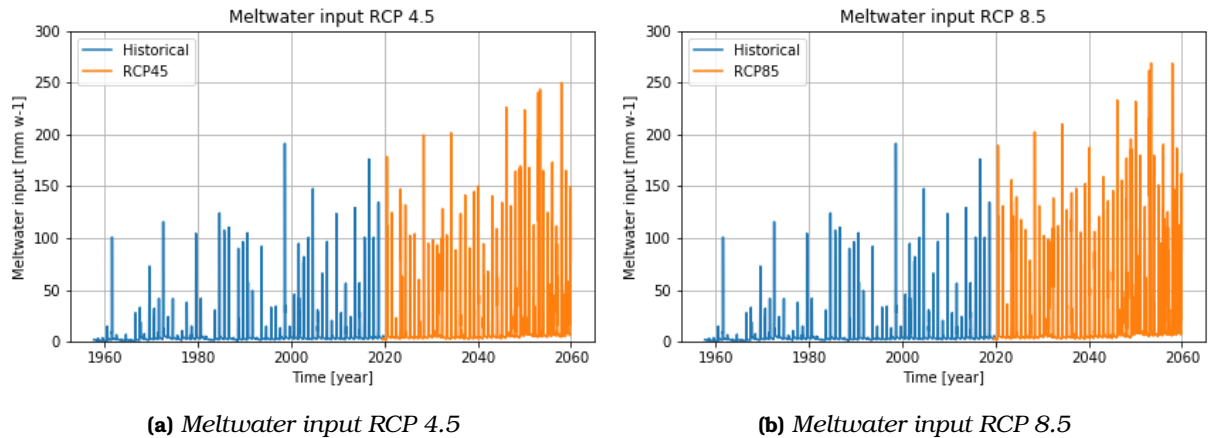
Figure 4.6: *Meltwater input for both future runs in mm per week, averaged over the full model grid.*

The depth of the EBFM grid changes slightly every time step due to compaction and densification of the layers. The evolution of the depth of five layers of the EBFM used in the firn aquifer model can be observed in Figures 4.7a and 4.7b. This obviously means that the depth at which density data is available changes as well, so in the LPFAM the vertical discretization should change every time step.

(a) *Depth evolution RCP 4.5*

(b) *Depth evolution RCP 8.5*
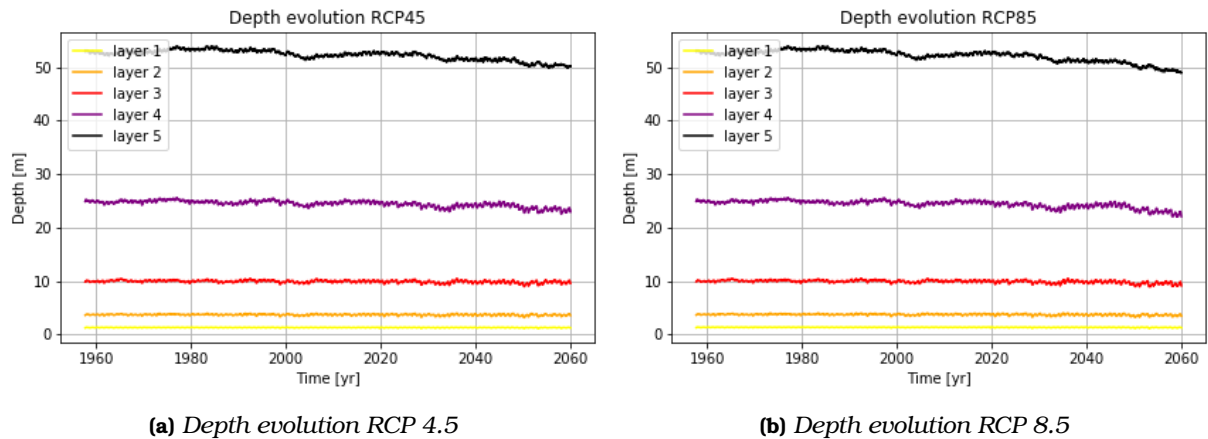
Figure 4.7: *Averaged depth of the five layers of the EBFM used in the firn aquifer model per time step for both the RCP 4.5 and the RCP 8.5 scenario*

4.4   Firn aquifer modelling - the LPFAM

MODFLOW 6 is chosen in this research to model the horizontal and vertical water flows in the PFA on the Lomonosovfonna ice cap. For an extensive documentation, the reader is referred to Langevin et al. (2017). MODFLOW 6 is a groundwater model developed by the U.S. Geological

Survey (USGS) and is coded in FORTRAN. MODFLOW 6 makes use of so-called 'input packages', that specify parts of the model. MODFLOW 6 includes static ('Steady') packages, those are packages that do not change during the simulation. Examples include the discretization-package (DIS) and the Output Control package (OC). Dynamic ('Transient') packages are time-dependent. Examples include the well package (WEL) and the constant head boundary package (CHB), every simulated timestep they can be changed. One can choose which input packages to use, and leave out unused ones, which increases simulation speed.

MODFLOW 6 uses the Newton-Raphson formulation to solve the set of equations that arises when Eq. 2.5 is applied on a discretized grid (Control Volume Finite Difference method). For an extensive documentation on the Newton-Raphson formulation and its development, I refer to Ypma (1995) and Ben-Israel (1966).
The Newton Raphson formulation is used to solve a set of differential equations in the form of Eq. 4.7, and the numerical solution is said to converge more often than previous formulations (Langevin et al., 2017).

$$J^{k-1}\Delta h^k = -r^{k-1} \tag{4.7}$$

In Eq. 4.7, J^{k-1} is the Jacobian matrix constructed using the head heights of time $k-1$, Δh^k the head update vector and r^{k-1} the residual vector. One can write Δh^k also as $h^k - h^{k-1}$, thereby turning Eq. 4.7 into Eq. 4.8.

$$J^{k-1}h^k = -r^{k-1} + J^{k-1}h^{k-1} \tag{4.8}$$

The goal of MODFLOW 6 is to use equation 4.8 with all heads from the previous time step ($k-1$), to obtain the heads of the next time step h^k. MODFLOW 6 uses an iterative process for that: every iteration a solution is tested, if it close enough to the previous solution, convergence is reached and the solution is accepted as 'final'. Convergence does not always happen, this will be discussed further in section 4.6.1.

There are three ways to construct input files for MODFLOW 6: by using a Graphical User Interface (GUI), by using packages embedded in programming languages and by writing the input files directly, either in for example IFortran or any text editor of choice. There are several GUI's available, commercial and free ones. Examples include DarcyLite and ModelMuse. The advantage of GUI's is the simplicity and readability of the input files, one can for example in ModelMuse visually build the grid and assign properties per cell. The disadvantage is the lack of complexity, GUI's are not suited to construct complex grids with different properties per cell. Constructing input files directly, gives most freedom, but is extremely labour intensive.

In this research, FloPy (developed by Bakker et al. (2018)) is chosen to construct the MODFLOW input files. The FloPy Python package can be used to construct input files, run MODFLOW, import MODFLOW output and postprocess and plot results, all in Python. FloPy offers the flexibility of creating input files directly, using Python, while being less labour intensive than writing the input packages by hand. The disadvantage of FloPy is the basic documentation, as the package is open sourced and developed and managed by volunteers. The input packages used to model the Lomonosovfonna PFA, as well as a small description on what they are used for, are presented in table 4.1.

The packages described in table 4.1 need input data. This can for example be one value (a so called 'float'), MODFLOW 6 will then use the float value for all grid cells, that are created using the DIS package. In this case, input files consists of matrices with values per grid cell. In the most memory-intensive case, the input matrices are 4D: 3D for every grid axis (rows, columns and layers) and one extra dimension for time, so that every time step a new data set for all cells can be used. Depth and Density from the EBFM are for example 4D matrices, as they change every time step for all cells.

Table 4.1: *Input packages used in the MODFLOW 6 model of the PFA on the Lomonosovfonna ice field. Steady packages are packages that do not change during a simulation period, Transient packages do change. The abbreviation is the abbreviaton used by MODFLOW and FloPy to identify the package.*

Package name	Abbreviation	Steady/Transient	Description
Simulation	SIM	Steady	Defines the simulation engine, MODFLOW 6 in this research
Groundwater Flow	GWF	Steady	Sets the environment for the model
Iterative Model Solution	IMS	Steady	Determines iterative solution options
Discreatization	DIS	Steady	Determines spatial discretization of the model
Initial Conditions	IC	Steady	Sets Initial conditions
Node Property Flow	NPF	Steady	Sets hydraulogic properties per cell
Time discretization	TDIS	Steady	Discretises time and stress periods
Storage	STO	Transient	Defines storage properties per cell
Time Varying Specified Head	CHD	Transient	Defines fixed boundaries in the model
Recharge	RCH	Transient	Defines the input of meltwater and percolation in the model
Output Control	OC	Steady	Defines what should be saved as output

MODFLOW 6 works with time steps and stress periods. Time steps can be any dimensions, chosen by the user. A MODFLOW 6 stress period is a set of time steps for which the transient packages shown in Table 4.1 remain constant. Stress periods of one time step therefore imply that for every time step the transient packages uses different input data. Large stress periods of multiple time steps might help run the model faster. However, this requires larger input files, and produces larger output files, that require more memory. Smaller time steps require smaller input files, and the solution might become more accurate, but the runtime increases significantly, as for each time step, new data needs to be read in. The basic MODFLOW 6 output is a binary file, containing per grid cell per time step the head height and flows in all directions. Postprocessing results in Python requires the output files of MODFLOW 6 not to exceed the memory limit of the Python engine.

As can be seen in Table 4.1, the packages NPF and DIS are steady, which means that they do not change during a MODFLOW simulation. In groundwater modelling, with for example solid porous media like rocks and sand, this can be a justifiable simplification. This is, in the case of modelling a PFA, not desired. During long runs (approximately ≥ 3 years), one could reasonably expect that the topography of the ice field changed, as well as density of the layers and therefore the hydraulic conductivity and storage. In the case of the Lomonosovfonna aquifer, the depth profile of the input data from the EBFM changes every time step, as can be observed in Figures 4.7a and 4.7b. Vertical discretization is governed by the 'DIS' package, so this static package should be time dependent. Also, as density changes every time step, the hydraulic conductivity needs to change as well. Hydraulic conductivity is defined in the 'NPF' package.

It is therefore needed to make separate MODFLOW 6 models every time step the steady packages need to change. To connect these separate MODFLOW 6 models into one model, the head heights of run t are used as initial conditions for run t+1. This allows steady packages to change per time step, but also as a way to make more efficient use of storage. Output can then be saved per time step, in separate blocks, instead of one big block at the end of one original MODFLOW simulation. Finally, this approach can be used to calculate processes in between simulations that are not part of the MODFLOW model, such as refreezing/thawing. This all can
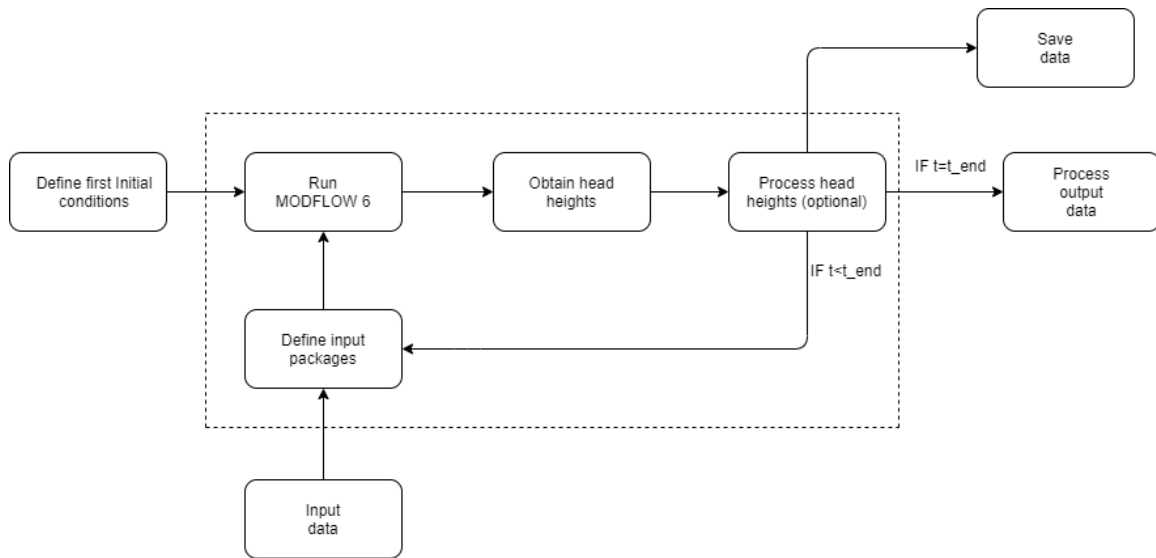
Figure 4.8: *The modelling process, in which every time step a new MODFLOW model is used, using the water table height from the previous time step as initial conditions. The dotted lines indicate the loop, for which every loop represents a new MODFLOW model, that uses the head height output of the previous loop as initial conditions. Note that input data can be read in every loop, instead of all at once, and that output data can be stored after each loop.*

be implemented by using a loop. A schematic overview of the modelling process is presented in Figure 4.8.

MODFLOW 6 is in essence a Darcy flow solver, and by using packages one can choose which physical processes are part of the simulation, and which not. Furthermore, the EBFM solves multiple physical processes to deliver the datasets that are input to the LPFAM, these processes are therefore indirectly part of the LPFAM as well. There are processes missing in the LPFAM, that might change the results or become the focus of further research. The three most important missing processes, mentioned in the literature, are 1) Firn - Aquifer interactions, 2) sinks and 3) aquifer refreezing. Firn-Aquifer interaction is the exchange of energy between the water and the surrounding firn. Also, a higher water table means generally that water is present in layers with a lower density, which contain more pore space and can therefore hold more water than lower layers. Therefore, as the water table rises, more mass of water is stored in the upper layers per [m] depth than in the lower layers, for the lowest density computed by the EBFM model (350 kg m^{-3}) this means that 62% of the volume of the layer is pore space. Therefore, per 350 kg of firn, there would be 620 kg of water if the layer would be completely saturated. It could be reasonably expected that the water significantly warms the cold firn close to the surface (to roughly 10 meters depth), where the firn is effected by the surface temperature, or compresses lower layers due to the water's weight.

Sinks in firn hydrology can be crevasses or moulins, that can drain water to the bed, away from the aquifer. No data is available on the existence, location, size and capacity of the sinks on the Lomonosovfonna, so they could not be added to the LPFAM. The only sink for water in the LPFAM is horizontal movement through the boundaries of the model domain. Sinks can be added in MODFLOW 6 using the WEL or DRN package.

Aquifer refreezing can happen if the surrounding firn is cold enough to freeze (part of) the water present in the pore spaces. This can decrease the water content and therefore the head height of the aquifer and increase the density of the firn. If the water table height is close enough to

the surface, where the cold wave during winter can penetrate, only the top of the water column might refreeze, creating a flat ice plate referred to as an 'ice lens'. This ice lens then entirely blocks the water table from rising, or meltwater from the surface to reach the aquifer, effectively creating a small confinement unit. The PFA is, if that occurs, not entirely unconfined, and the packages STO and NPF (see Table 4.1) need to be entirely redefined. There is evidence of ice lens formation on the Lomonsovfonna, in the form of an discontinuous density profiles (Marchenko et al., 2019), but no spatial data was available for this study, so this is not a part of the LPFAM. A coupled EBFM - LPFAM, where the water can exchange heat with the firn, and eventually refreeze and become part of the firn, could be the scope for further research to incorporate ice lens formation and the effects they have on PFA formation.

An overview of what processes are taken into account in the EBFM and the LPFAM, and the most important physical processes that are not part of the two models, is presented in Table 4.2.

Table 4.2: *Physical processes included in the EBFM and the LPFAM.*

Part of the EBFM	Part of the LPFAM	Not included
Solving Energy Balance	Horizontal flow	Firn - Aquifer interactions
Thermodynamics: heat conduction	Vertical flow	Sinks (crevasses, moulins)
Thermodynamics: refreezing vertical percolating water	Storage in pore spaces	Aquifer refreezing and ice lens formation
Densification: gravitational packing	Head height evolution	
Densification: refreezing vertical percolating water		

4.5   Analyzing the MODFLOW output - tuning process

The MODFLOW output data is first checked qualitatively using a contour plot, to assess if the values are reasonable, and did not reach or went above the surface. In those cases, MOD-FLOW creates an extra 'above surface' layer with default settings. If that happens during the simulation, the output values cannot be trusted anymore (Langevin et al., 2017). Between all time steps, in the 'Process head heights(optional)' box in Figure 4.8, it is checked if the water table exceeds the surface height. If the water table exceeds the surface height, the water table height is set to the surface height, therefore discarding the water column above the surface, effectively assuming that the water above the surface would runoff immediately. Those events are counted. It proved that the water table height only exceeds the surface in the future runs, so this was not an issue in the tuning process, which is done with historical data (1957 - 2017).

After a full simulation run (1957 - 2017), the model output is compared to the observations. An example of the positions of observational data with respect to the model grid is shown in Figure 4.9. If a modelled grid point (blue pentacles in Figure 4.9) is closest to more than one observation point (orange dots), the mean of the water table depth and position of the group of closest observations is taken and linked to the modelled grid point. Then, the Root Mean Square Error (RMSE), Pearsons Correlation Coefficient (R-value) and the mean bias are calculated between the closest modelled grid points and the observations. The R-value will give an estimate of the match of the shape of the modelled grid with the observations, the RMSE will give an indication of the difference between the modelled output and the observations, and the bias will give an indication if the model produces generally too low or too high values compared to the observations. The RMSE is used as primary indicator of the quality of the run.
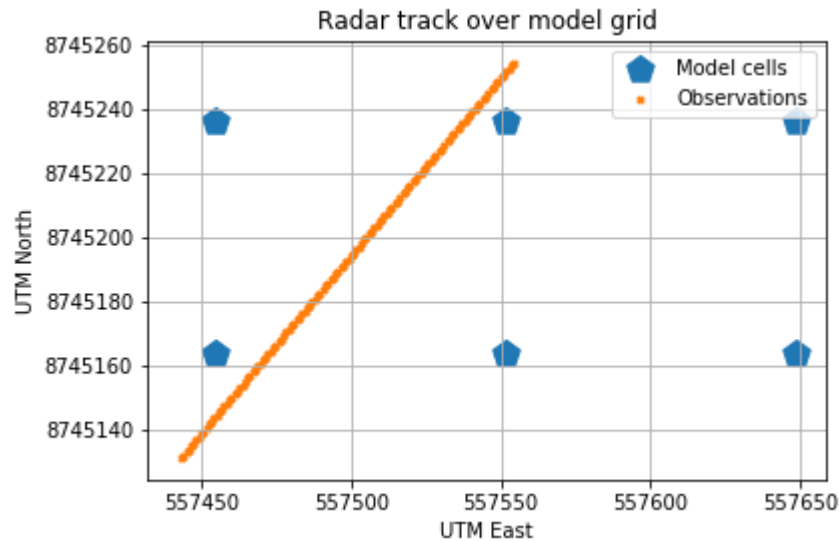
Figure 4.9: *Example of the modelled grid data poinst (blue pentangles) compared to data from a radar track (orange dots)*

4.6 Model setup & experiments

The LPFAM is run from the beginning of the EBFM dataset, August 1957, to the date of the observations, April 2017, with a weekly resolution. These runs were used to test different initial and boundary conditions, and the model sensitivity. The setup process was done in three steps: 1) ensuring model convergence, 2) finding appropriate initial and boundary conditions and 3) find the hydraulic conductivity distribution for which the modelled head heights are closest to the observations.

4.6.1 Model convergence

Step one is to find fitting parameter settings for MODFLOW to converge. As described in section 4.4, MODFLOW 6 solves Eq. 4.8 using iterations, it does that by testing a solution, assess if the difference with the previous solution increases or decreases and accordingly discards or keep the new solution. If the difference between two solution-finder runs (called 'inner iterations') is below a certain threshold, MODFLOW 6 accepts the solution as final. A final solution can therefore only be found if the difference between inner iterations decreases: referred to as 'convergence'. For complex models, MODFLOW 6 is not always able to converge. There are multiple parameters one can change to increase the chance of convergence, often sacrificing some accuracy in the final solution, and a fitting set of values is model-specific and needs to be determined in a trail-and-error process according to Langevin et al. (2017). If MODFLOW 6 does not reach convergence, the model terminates with an error.

Using the Newton-Raphson formulation instead of the classical formulation to solve equation 4.8, makes it easier for rewetting and drying to happen. The classic formulation 'checked' per inner-iteration if a cell is dry or not. If the cell is dry, it is regarded as inactive (and given a default inactive head height of 1E-30), and it will only rewet if the cells nearby have a head height higher than a specified threshold. The disadvantage of this method is that MODFLOW checks each cell multiple times per time step, which makes it possible for a cell to rewet and dry more than once in a time step. Also, if the conditions in the neighbouring cells are suffi-cient, the cell could end-up in an endless rewet-dry-rewet cycle, preventing convergence. The

Newton-Raphson formulation does not require cells to be inactive when dried up, keeping the head height of the cell at the cell bottom, which makes it more suitable for simulations where rewetting and drying could happen. It is furthermore important that resolution and hydraulic conductivity are in the same order of magnitude, to prevent the water from flowing through the whole grid in one time step.

The most important constraint in this research for convergence proved to be a combination between hydraulic conductivity and cell dimensions. If the hydraulic conductivity is large and the cell dimensions small (e.g. a high-resolution grid), the water could pass through multiple cells in one time-step. This is not per definition wrong, MODFLOW 6 can handle water passing through multiple cells in one time step, but for a certain combination of hydraulic conductivity and cell size, the model did not converge anymore, because too much cells were passed by the water. Since hydraulic conductivity was used as a tuning parameter in this research, cell size needed to be fitting for all tuning experiments. By trail and error, it proved that cell dimensions of 96 x 72 meters (x,y) worked for all tuning experiments.

4.6.2   Initial and boundary conditions

Step two is to find appropriate initial and boundary conditions, and a timescale for which the model does not 'feel' the initial conditions anymore. A bufferzone, between the observational grid and the edge of the grid, is constructed to neutralize the effect of the boundary conditions on the water table heights in the model grid. Different bufferzone sizes were tested. For every bufferzone-size experiments, three experiments were conducted: the head height at the outer boundary of the bufferzone was fixed at 1, 10 and 20 meters above the bottom of the model grid. The model was then run for 30 years (1987 - 2017) with arbitrary initial conditions (5 meters above the bottom of the model grid). If the head height did not change for all three experiments, the bufferzone was seen as 'safe'. It is found that the bufferzone should be roughly 1.5 times the size of the grid containing the measurement tracks. A smaller bufferzone made the water table depths in the measurement-track grid dependent on the boundaries. A larger bufferzone is possible, but this will either decrease the resolution or increase the run-time of the model. The boundary of the bufferzone has a fixed water table height of 10 meters above the bottom of the vertical grid. No water in the boundary is not allowed by MODFLOW's boundary package (CHD in table 4.1), and using a water table higher than 20 meters above the depth of the lower layer will cause the water table to reach the surface of the bufferzone, for some experiments with a low hydraulic conductivity, and therefore make the model and the spin-up run unreliable.

As first try the initial conditions were chosen to be a water table that is 5 meters above the bottom of the vertical grid. Tests with a uniform hydraulic conductivity and no water input were performed to see when the modelled water table height as function of the time became constant, with the previously described boundary conditions. This happened after 20-25 years for the lowest hydraulic conductivity. Therefore, a spin-up of 30 years, to be absolutely sure the initial conditions do not influence the model experiments, with repeated 1957 conditions was performed, using the most fitting hydraulic conductivity and the optimized bufferzone.

4.6.3   Model tuning experiments

Step three is to tune the model to produce water table heights close to the observations by changing the hydraulic conductivity, using the found fitting initial and boundary conditions from the previous steps and using the RMSE as a fitting indicator. From the output of the last time step, the RMSE, Pearson's R and the bias are determined between the observed and the modelled head heights. The RMSE is used as a primary indicator: the model tuning experiment with the lowest RMSE is regarded as the best run. Bias and Pearson's R are used as secondary indicators.

Three different distributions of the hydraulic conductivity were tested: Uniform for all layers, third polynomial density-hydraulic conductivity function and the Kozeny-Carman distribution as given in Eq. 2.6. For the simulation runs to tune the model (1957 - 2017), the density does not change much, as can be seen in Figure 4.5a or 4.5b. For both RCP scenarios, the average density increases significantly. We therefore argue that the hydraulic conductivity probably needs to be dependent on the density for the future runs, which justifies the use of hydraulic conductivity-density functions.

The results of the sensitivity runs are presented in the next chapter, chapter 5. Experiments were also done on the sensitivity of the LPFAM to crevasses, changing the vertical resolution, and the usage of a cutoff density. The results are summarized in section 5.3. A schematic summary of the full tuning process, from input data to the EBFM to output head heights and the corresponding statistical parameters, is presented in Figure 4.10.
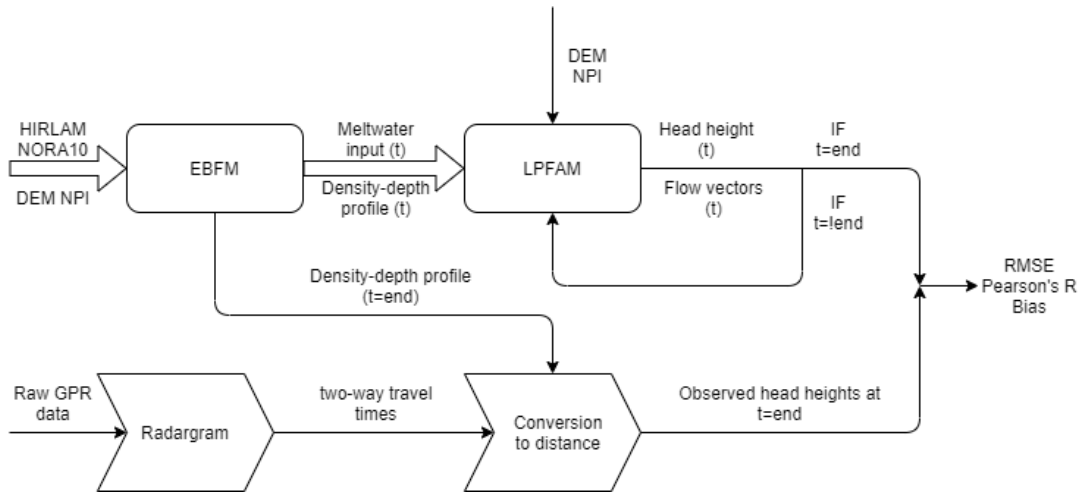

Figure 4.10: *Schematic overview the model tuning process. Rounded square represent model steps, indented arrows indicate processing of observations. (t) refers to time-dependent variables. t=end is the last time step of the model and correspondents to the moment the observations were made, April 2017. Firn density-depth profile(t), Meltwater input (t) and the DEM are first interpolated before entering the Lomos FAQM, in the way described in section 4.3. The IF t=end vs IF t=!end refers to the loop presented in Figure 4.8*

Then, using the results of the three tuning steps, a spin-up was done to obtain initial conditions for the year 1957, by letting the model run for the determined initial conditions timescale of 30 years. Then, with suitable boundary conditions, initial conditions and the best hydraulic conductivity, and using the spin-up as initial conditions, three model experiments were conducted.

4.6.4 Model experiments

Three experiments were conducted, using the tuned model after completion of the before described steps: one historical run (1957 - 2019) using data from van Pelt et al. (2019), one future run (2019 - 2060) using RCP 4.5 input data from the EBFM and one future run (2019 - 2060) using RCP 8.5 input data. The EBFM data for the RCP runs (2019 - 2060) is unpublished, but the same model set up as for the historical run described in van Pelt et al. (2019) is used, with forcing from the Arctic CORDEX project, which is dynamically downscaled CMIP 5 data (Bilt et al., 2019). For an elaborate description of the Representative Concentration Pathways, the reader is referred to Van Vuuren et al. (2011). Results from the historical run will be used to

assess the dynamics of the aquifer in the past, and results from the two future runs will be used to assess the response of the perennial firn aquifer to a changing climate.

In this chapter the results of the tuning process are shown. The results are sorted per distribution of the hydraulic conductivity, starting with the third order polynomial hydraulic conductivity-density function in section 5.1, followed by the Kozeny-Carman distribution and the uniform hydraulic conductivity distributions in section 5.2. Then, three more sensitivity runs are discussed in section 5.3: a run including sinks to represent crevasses, one with an increased vertical resolution, and one using a cutoff density.

The model was run from august 1957 to April 2017. Initial conditions are chosen to be lower boundary of the model + 10 meters, boundary conditions consists of a bufferzone roughly 1.5 times the observation grid, with a fixed head height of 10 meters above the lower boundary of the model. As benchmark values the for hydraulic conductivity, the minimum and maximum value of recent measurements were used (from Miller et al. (2017)), respectively $2.5*10^{-5}$ m/s (15.12 m/week) and $1.1*10^{-3}$ m/s (665.3 m/week).

Physically, one would expect the hydraulic conductivity to be dependent on density. A denser medium, has less pore spaces and less space for water to flow through and is therefore expected to have a lower hydraulic conductivity. Furthermore, as the density of the firn approaches the density of ice, the effect is expected to be stronger, as some pores might no longer be connected to each other and thereby completely stop the flow. To capture this effect, we performed tests with a third order polynomial, that is almost constant for densities between 350 and 600 kgm^{-3} and decreases to the minimum value of the hydraulic conductivity given in the literature.

5.1 Third order polynomial

First, a third order polynomial was constructed between the maximum and minimum value of the hydraulic conductivity found in the literature, and the average minimum and maximum density of the LPFAM for the period 1957 - 2017. Then, the whole polynomial was multiplied with a factor to change its shape. Twenty of such functions were tested, and a selection of different third order polynomial hydraulic conductivity-density functions are shown in Figure 5.1. Because the density can get higher than 830 kg m^{-3}, especially in the future scenarios, and some polynomials produce hydraulic conductivity's equal to or lower than zero for a high density, the lowest value for the hydraulic conductivity is fixed to be the minimum value found in the literature.

The resulting RMSE, Bias, the best fit compared to the observations and the error are shown in Figures 5.2 and 5.3.
The RMSE reaches a minimum for a factor of 2.4, which corresponds to a hydraulic conductivity function shown in Eq. 5.1, in which K is the hydraulic conductivity and ρ the firn density.

$$K = -5.76 \times 10^{-5}\rho^3 + 8.46 \times 10^{-2}\rho^2 - 4.09 \times 10^1\rho + 8.36 \times 10^3 \tag{5.1}$$

The GPR could not detect a water table at greater depths than 35 meters. The LPFAM produces water tables in the western part of the grid that are around 40 meters below the surface, which is in line with the missing observations, but could not be tested and therefore it is not taken into account in the RMSE. The same applies for the large spot with a deep water table (yellow) in the south-western part of the model where the observation line is interrupted: if the water table in reality is as deep as the model predicts, the GPR would not be able to detect it. This again points out that the model likely calculates representative head heights in that area, but they could not be used in RMSE-calculations, so the RMSE calculated here might be an overestimation.
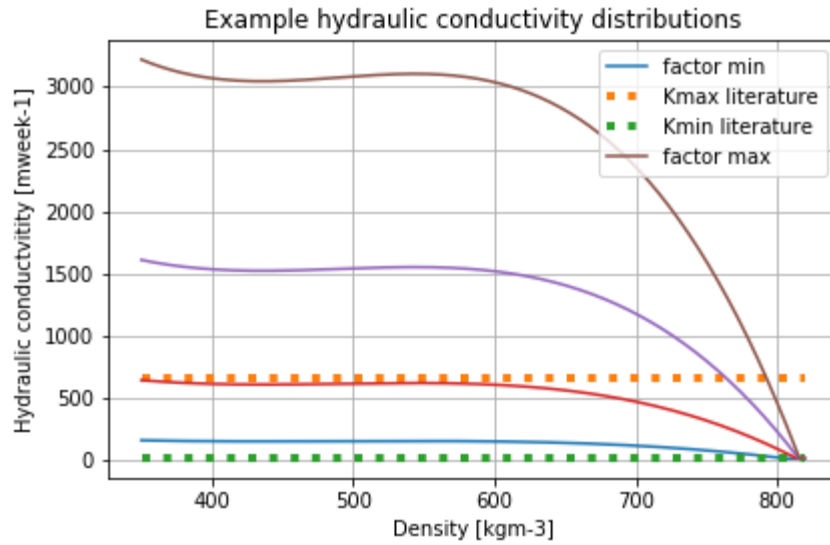
Figure 5.1: *Four examples of hydraulic conductivity distributions that were tested. The original polynomial (red) is multiplied with a factor between 0.2 (factor min) and 5 (factor max)*

(a) *RMSE and bias*

(b) *Observations vs model*
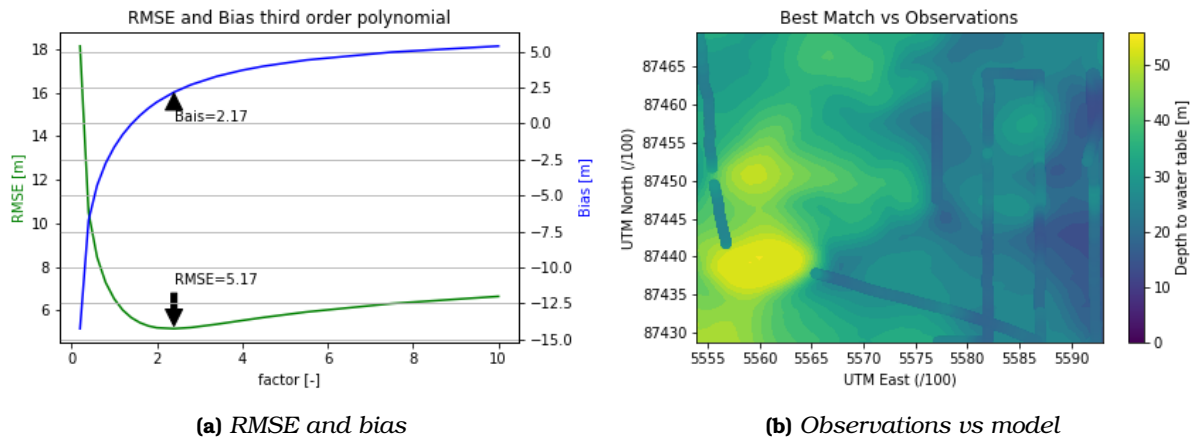
Figure 5.2: *Figure 5.2a: Bias (blue) and RMSE (green) for all tuning experiments, with the lowest RMSE obtained highlighted with the corresponding bias. Figure 5.2b: Observations data plotted over the lowest-RMSE modelled water table. The closer the colors, the closer the modelled water table height is to the observations*

(a) *Error*   **(b)** *Pearson's R*
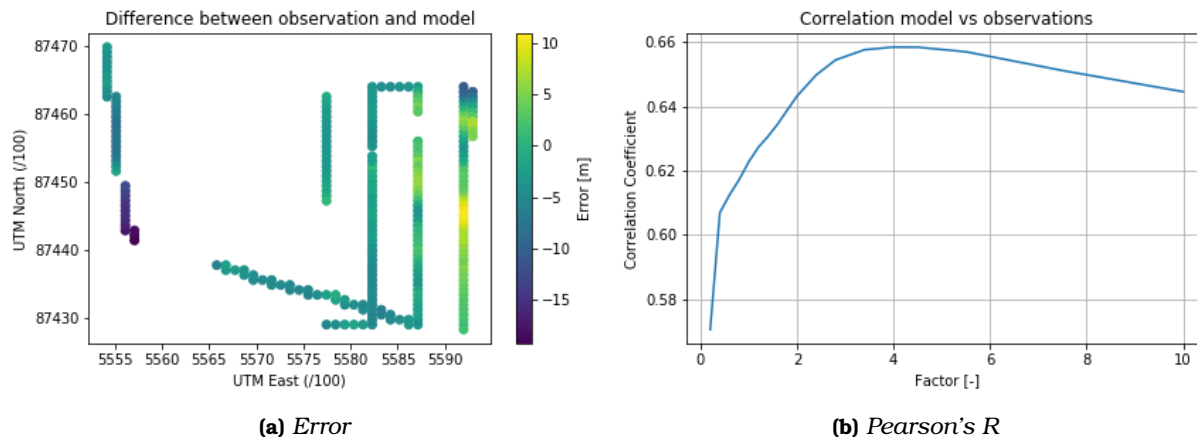
Figure 5.3: *Figure 5.3a: Difference between the lowest-RMSE modelled water table and observations. Positive values indicate a modelled water table height that exceeds the observations, and vice versa. Figure 5.3b: Pearon's R for all third-order polynomial tuning experiments*

Pearon's R has a value of ±0.65 for a multiplication factor of 2.4, which is not the maximum. Pearon's R increases sharply for low factors, but does not change significantly for higher factors. This gives rise to the notion that, once the hydraulic conductivity is above a certain threshold, it does not influence the shape of the water table anymore. It is expected that from that point, the dominant effects on the shape of the water table are the elevation profile (determines the bottom slope) and the density (determines the storage per cell).

The model produces a water table that is too deep near the southern local peak (see Figure 3.2), and too close to the surface at a small section of the most eastern observation track, see Figure 5.3a. The error near the southern peak could be caused by a local effect that holds the water as it drains away from the peak, such as a local dense spot of ice in the firn that is not part of the EBFM density profile and therefore not part of the LPFAM. The overshooting of the model in the eastern observations track could be because of the lack of crevasses. The area to the east of the grid is said to contain crevasses by the team carrying out observations, but no data on size and spot is available, so it could not be added. Adding crevasses adds a drain in the model, which will locally lower the water table.

5.2 Kozeny-Carman and uniform distributions

The Kozeny-Carman equation, shown in Equation 2.6 was tested using the parameters C_{KC} and D_{10} multiplied by a factor as tuning. Some KC-distributions are presented in Figure 5.4. As can be seen in Figure 5.5, a minimum RMSE of 9 meters is reached for a factor of 30, which is considerably higher than for the polynomial fit. The errors shown in Figure 5.6 show the same pattern (negative in the western part, positive in the eastern part), but are more pronounced compared to the polynomial fit. Pearson's R is 0.615 for the best run slightly lower than the one of the best polynomial run. The fact that the RMSE is considerably higher and the fact that Pearson's R does not differ much confirms that, from a certain hydraulic conductivity onward, it does not determine the shape of the water table anymore.

Tests have been done using a uniform hydraulic conductivity over the whole grid, ranging from K_{min} to K_{max}. The resulting RMSE, Bias, best fit contour, error and Pearon's R are presented in Figures 5.7 and 5.8. Clearly, the uniform distribution performs poorly, with large errors and an RMSE of 12.82 meters at minimum.
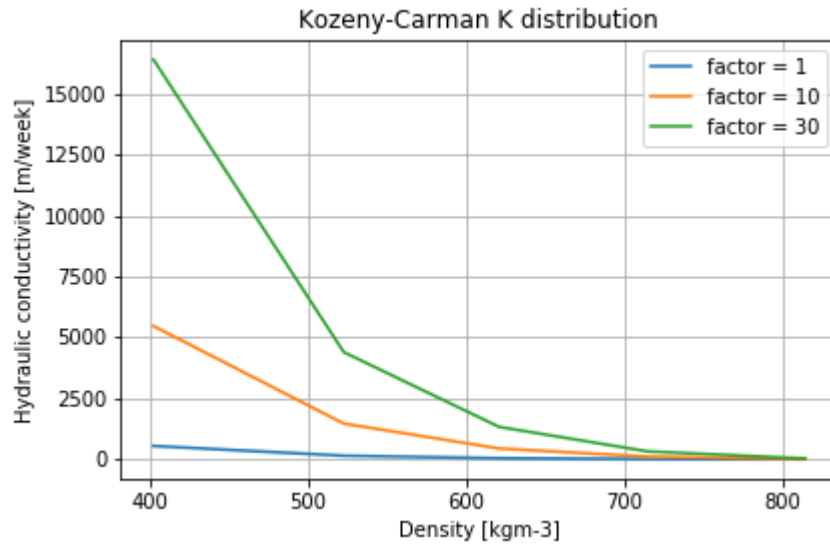
Figure 5.4: *Three examples of a Kozeny-Carman fit*
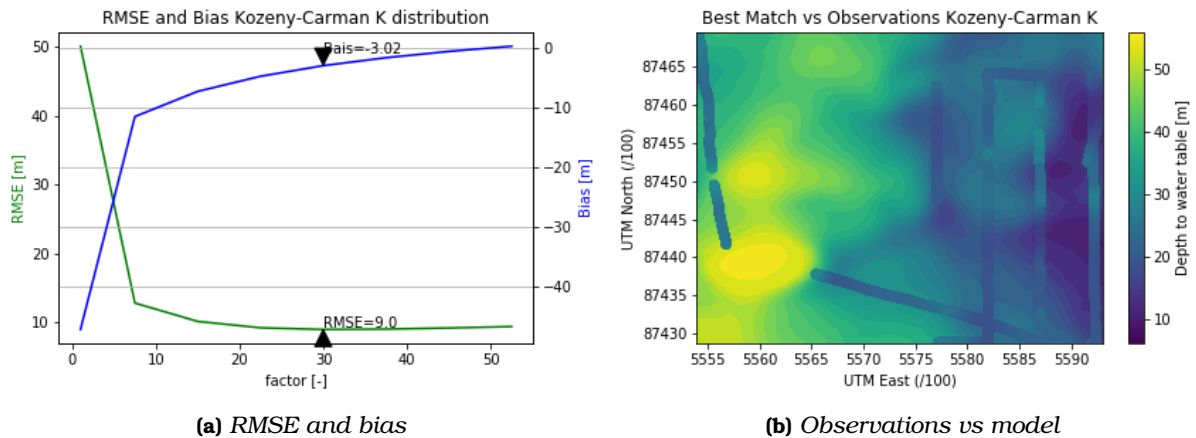
(a) *RMSE and bias*

(b) *Observations vs model*

Figure 5.5: *Figure 5.5a: Bias (blue) and RMSE (green) for all Kozeny-Carman tuning experiments, with the lowest RMSE obtained highlighted with the corresponding bias. Figure 5.5b: Observations data plotted over the lowest-RMSE modelled water table. The closer the colors, the closer the modelled water table height is to the observations.*

(a) *RMSE and bias*

(b) *Observations vs model*

Figure 5.6: *Figure 5.6a: Difference between the lowest-RMSE modelled water table and observations for the Kozeny-Carman tuning process. Positive values indicate a modelled water table height that exceeds the observations, and vice versa. Figure 5.6b: Pearon's R for all third-order polynomial tuning experiments*

(a) *RMSE and bias*

(b) *Observations vs model*
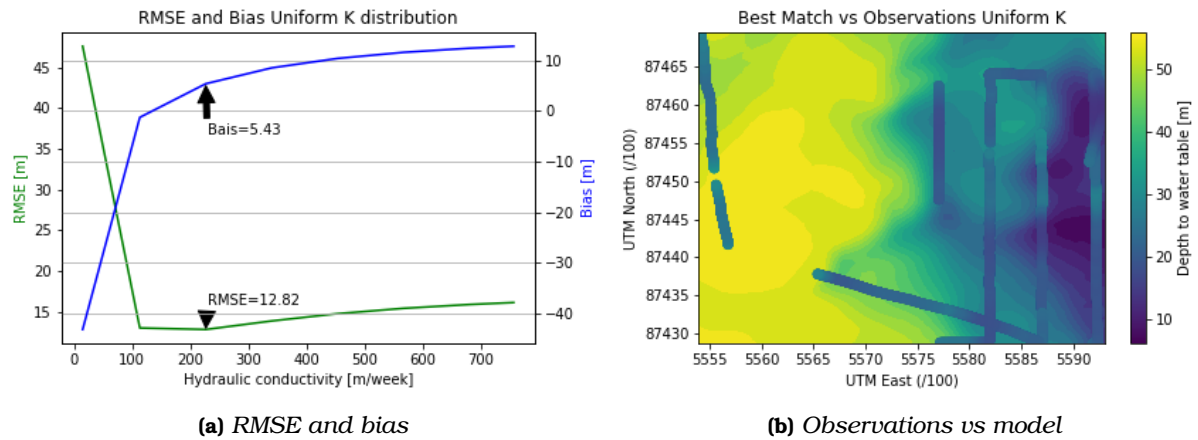
Figure 5.7: *Figure 5.7a: Bias (blue) and RMSE (green) for all uniform tuning experiments, with the lowest RMSE obtained highlighted with the corresponding bias. Figure 5.7b: Observations data plotted over the lowest-RMSE modelled water table. The closer the colors, the closer the modelled water table height is to the observations.*
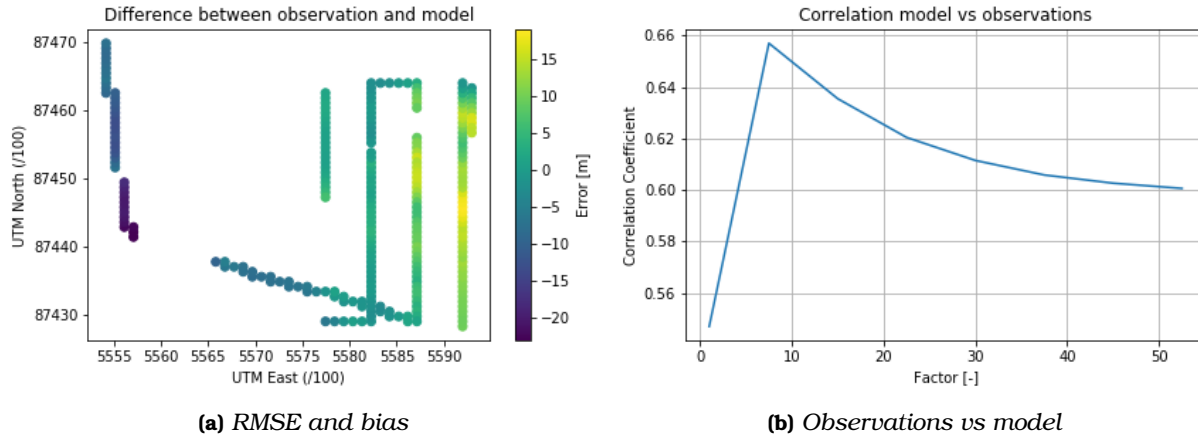
(a) *RMSE and bias* **(b)** *Observations vs model*

Figure 5.8: *Figure 5.8a: Difference between the lowest-RMSE modelled water table and observations for the uniform tuning process. Positive values indicate a modelled water table height that exceeds the observations, and vice versa. Figure 5.8b: Pearon's R for all third-order polynomial tuning experiments*
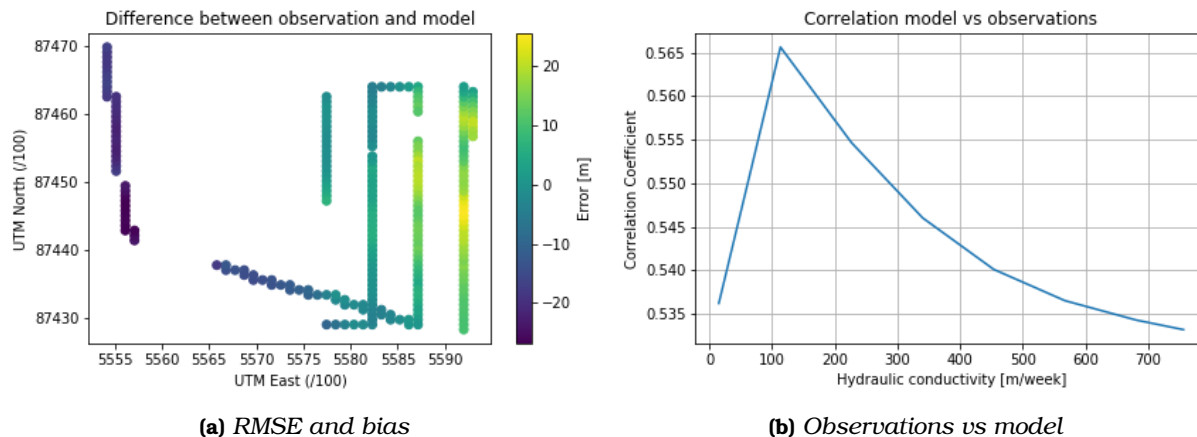
5.3 Crevasses, vertical resolution and cut-off density

It is, as described above, expected that there are crevasses present near the model grid on the Lomonosovfonna ice cap, but data lacks to make an accurate representation in the LPFAM. The effect of adding crevasses to different spots in the model grid was tested. The MODFLOW 6 package DRN (drain) was used to do this. The DRN package requires three input parameters: the position of the grid cell(s) of the drain(s), the water table height in the drain(s) and the hydraulic conductivity of the drain(s). Two cases were tested: one where a drain was added in the eastern bufferzone, next to the overshooting places in the tuning experiments, and one in the model grid in the gap of the second most eastern observational track. Adding a drain in the bufferzone had no significant effects on the modelled water table heights inside the grid. Adding a drain in the grid, and redoing the tuning process of the polynomial hydraulic conductivity distribution, changed the ideal factor from 2.4 to 1.6, making the average hydraulic conductivity lower, and resulted in a slightly lower RMSE of 4.9 meters, and a slightly higher Pearson's R of 0.71. Adding a drain therefore made the ideal hydraulic conductivity distribution closer to the values found in the literature, and the RMSE slightly lower.

The LPFAM has 5 layers, corresponding to layer 15, 30, 45, 60 and 75 of the EBFM. A test was done with 15 layers in the LPFAM, in which every LPFAM layer corresponds to every 5th layer of the EBFM. This did not significantly change the calculated water table heights, but it increased the computation time of the model experiments from 8 to 25 hours. Ideally, one would want the LPFAM to have the same vertical distribution as the EBFM, being 75 layers, also in further research if the two models will be coupled (this will be discussed in chapter 7). This will likely result in computation times of the LPFAM of 125+ hours, which was too long for this research. Since increasing the resolution did not significantly change the results of the LPFAM, five layers were used in the model experiments.

One could argue that for certain densities close to the density of ice, the pores will not be connected anymore and there will be no flow. Kuipers-Munneke et al. (2015) for example use a so called 'close-off' or 'cutoff' density of 830 kg m^{-3}. When the LPFAM is run with a pore close-off density, water table heights increase more in both future scenarios, and the annual variability increases as well. The residence time, presented and calculated in section 6.4, showed a very sharp decline, as soon as certain LPFAM model columns contained only cells

with a density higher than the cutoff density.

We believe that it would be better to add as few shocks in the model as possible, if the density of a model layer in one timestep increases from below 830 kg m^{-3} to above it, the layer suddenly becomes static: it can no longer store water and water cannot move through it, causing a jump in the water table height. There is no consensus in the literature about the usage of a pore close-off density. For example, the EBFM-model from van Pelt et al. (2019), where most of the input data for the LPFAM originates from, does not include a pore close-off density (van Pelt et al., 2012). To be consistent with the dataset from the EBFM, no pore close-off density is used in the LPFAM either.

In this section, the results of the historical and the future runs are presented. This chapter starts with a description of the climate of Svalbard in section 6.1, that is used as forcing for the LPFAM, to serve as background to explain the results from the model. Then, in section 6.2, the general results (mean, minimum and maximum water table depth evolution) of all three runs is discussed, as well as the time and counts at which the water table reaches the surface. Following up in section 6.3, a short period in all runs was picked and the effect of meltwater input is qualitatively discussed. Then, in section 6.4, the flow characteristics of the modelled PFA, being flow magnitude, direction and residence times, are presented and discussed. To conclude, in section 6.5 the correlation coefficients are presented between model input and model output. Some physical explanation of the results are given in this chapter, a more in depth discussion of the results is presented in chapter 7.

6.1   Climate on Svalbard

The temperature and precipitation mean and trend (1957 - 2019) of the forcing data, used for the historical run, are presented in Figure 6.1. As can be seen in Figure 6.1a, the mean temperature at the Lomonosovfonna ice cap is ±-15 C°. Accumulation rates at the Lomonosovfonna ice cap range between 1.2 - 1.8 m.w.e. a^{-1}. The temperature difference between summer and winter on Svalbard is ±30 °C (see for example the AWS measurements of the Lomonosovfonna from Pfeffer et al. (2018)). According to the model study of Kuipers-Munneke et al. (2014), a high accumulation rate and high temperature amplitude favour the formation of PFA's. Kuipers-Munneke et al. (2014) did a sensitivity analysis of accumulation rate and the annual temperature amplitude on the size of the vertical water column at the end of the winter. Their results, with conditions on the Lomonosovfonna ice cap highlighted, can be observed in Figure 6.2. Conditions on the Lomonosovfonna ice cap and the GrIS are comparable, and according to the model study by Kuipers-Munneke et al. (2014), a vertical water column can persist through the winter on the Lomonosovfonna ice cap.

A longer temperature trend, obtained from measurements at Longyearbyen airport, is shown in Figure 6.3, which also shows the different climate regimes obtained from the annual average temperature by using the Rodionov test. The EBFM data has a +0.4 °C bias and a 0.97 correlation coefficient with the temperature dataset shown in Figure 6.3 (van Pelt et al., 2019).

The temperature and precipitation trends for central Svalbard, where the Lomonosovfonna ice cap is situated, are presented in Figure 6.4. The RCP 8.5 scenario, being the scenario with the highest increase in emissions, shows for both temperature and precipitation generally a stronger trend compared to the RCP 4.5 scenario. However, the variability is also larger, the low boundary for temperature change in JJA and SON is lower in the RCP 8.5 scenario compared to the RCP 4.5. The same applies for the precipitation trends: all values are positive, and generally the precipitation increase is more pronounced and the variability is larger in the RCP 8.5 compared to the RCP 4.5 scenario. Both the precipitation and temperature increase are the largest during the winter, which is likely caused by combinations of a retreating sea ice cover and associated feedbacks (Arctic amplification). Bintanja and Andry (2017) have shown in a model study that during the 21st century the precipitation regime will shift from snow-dominated to rain-dominated, with the strongest increase in rain-on-snow events during the summer. Peeters et al. (2019) found a threefold increase in the rain events during the winter at the end of the 21st century compared to 2017, and Hansen et al. (2014) found in general that rain-on-snow events will increase through the 21st century.
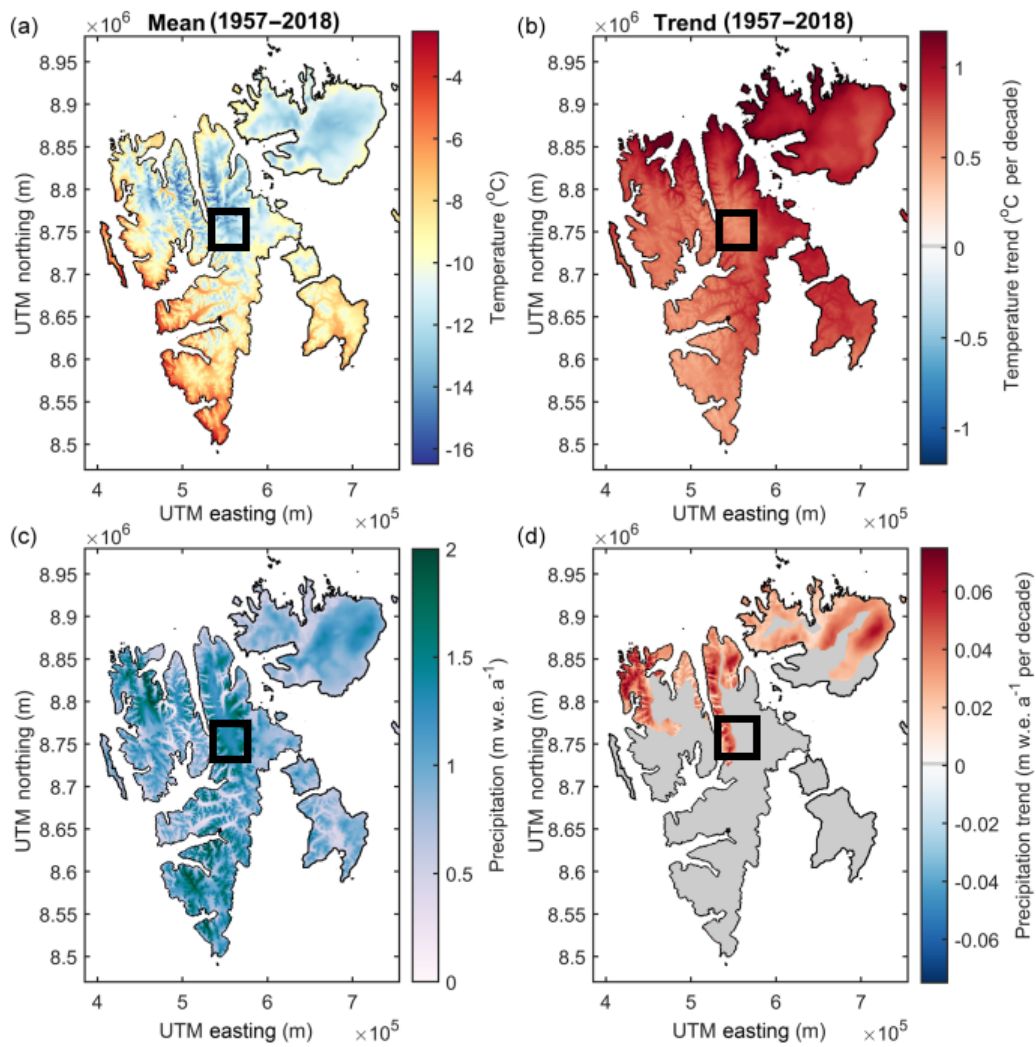
Figure 6.1: *Temperature and precipitation trends (1957 - 2019), from van Pelt et al. (2019). The black squares highlight the Lomonosovfonna ice field.*
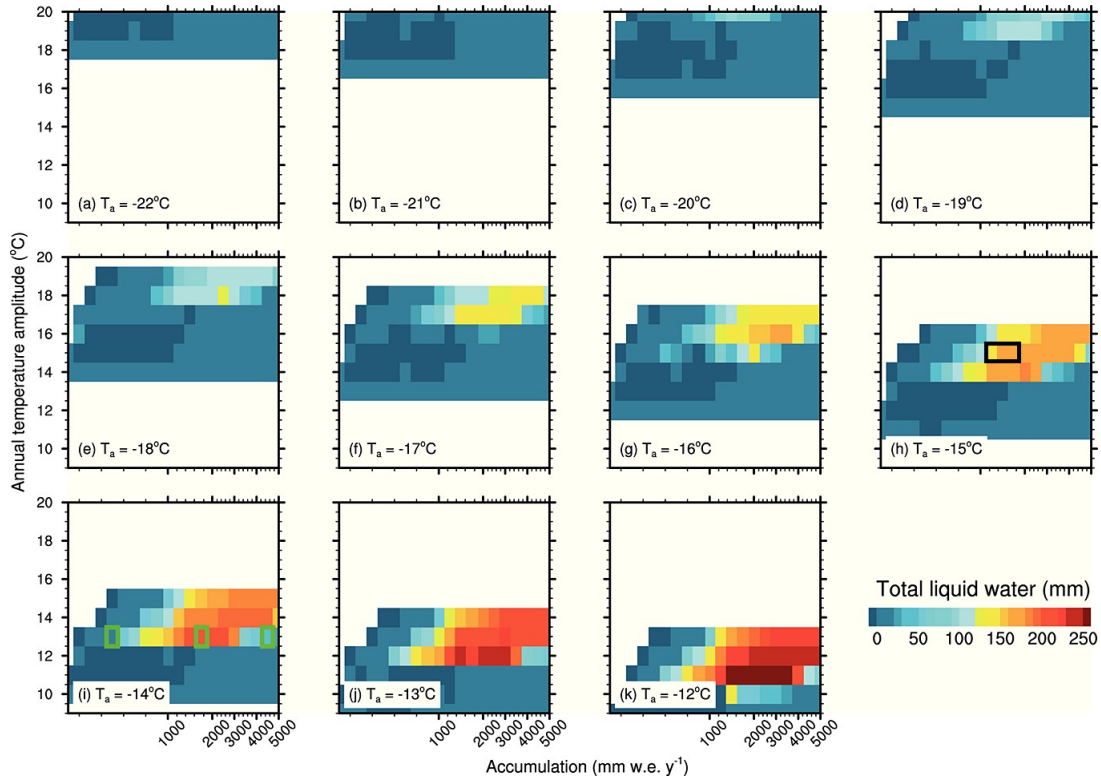
Figure 6.2: *The results of the sensitivity analysis of Kuipers-Munneke et al. (2014). Accumulation is for all figures on the x-axis, annual temperature amplitude is shown on the y-axis and the different subfigures present the results for different average annual temperatures T_a. In Figure 6.2i, the green squares represent the conditions on the study sites on the GrIS used in their research. In Figure 6.2h, the black square represent the conditions on the Lomonsovfonna ice cap*
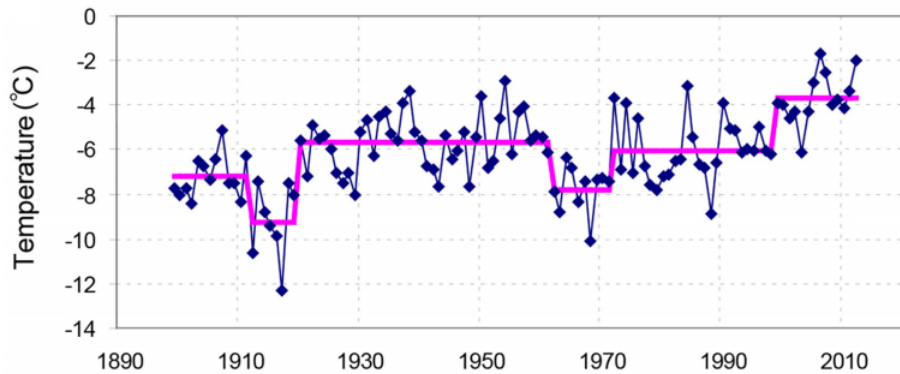
Figure 6.3: *Temperature observations annual mean at Longyearbyen airport, taken from Nordli et al. (2014). The purple line indicates a temperature regime, determined by the Rodionov test, see Rodionov (2004)*

Temp. change [°C]	1971-2000 to 2031-2060					
	RCP4.5			RCP8.5		
	Med	Low	High	Med	Low	High
Svalbard land area						
Annual	4.9	4.3	7.1	5.5	4.4	8.7
DJF	7.1	5.7	10.3	7.9	6.8	13.3
MAM	4.4	3.1	6.9	4.9	4	7.7
JJA	2.3	1.6	3.6	3.1	1.2	3.9
SON	5.5	5.3	8.2	6.5	4.5	10.2

(a) *Temperature change (°C)*

Precip. change [%]	1971-2000 to 2031-2060					
	RCP4.5			RCP8.5		
	Med	Low	High	Med	Low	High
Svalbard land area						
Annual	27	20	44	33	16	49
DJF	33	15	62	40	19	72
MAM	30	16	44	34	12	44
JJA	21	13	25	26	8	35
SON	26	25	44	35	15	53

(b) *Precipitation change(%)*

Figure 6.4: *Projected temperature (Figure 6.4a) and precipitation changes (Figure 6.4b) for the Svalbard land area for RCP scenario 4.5 and 8.5 from the Arctic CORDEX dataset, which is also used as input for the future runs of the EBFM. Figures taken from Hanssen-Bauer et al. (2019)*

6.2   Water table height

The resulting annual and spatial mean, standard deviation of the mean, maximum and minimum for every year of the three experiments are shown in Figure 6.5, in both Figures the RCP scenario is linked to the historical run. In all three experiments there is a substantial increase in the water table height. In the historical run (1957 - 2019), this increase is ±10 meters, which is 16 centimeters per year. In the RCP 4.5 run and the RCP 8.5 run, the increase is ±12.5 meters (30 centimeters per year) and ±20 meters (49 centimeters per year) respectively. Both future scenarios experience an accelerated increase from 2045. The seasonal amplitude (the difference between the annual minimum and the annual maximum) increases in the historical run from ±1.5 meters in 1960 to ±2.5 meters in 2019. The seasonal amplitude in the future scenarios are slightly larger, being ±3 meters around 2035. The increased water table height and variability is likely caused by the an increase in density and meltwater input, which will be discussed below. There is a sharp decrease to a local dip visible in the beginning of the 2050's. This coincides with a dip in density, which happens in both scenarios, see Figures 4.5a and 4.5b.

The increase in the water table height can be explained by three phenomena. First, the density increases, as can be observed in Figures 4.5a and 4.5b. This makes that there is less pore space available, and therefore less water can be stored in every layer. This means that the same meltwater input in firn with a higher density causes the water table to increase more compared to firn with a lower density. Increased density means therefore a higher water table. The hydraulic conductivity is density-dependent, and a higher density means a lower hydraulic conductivity. A lower hydraulic conductivity means less flow and more water piling up per vertical column, leading also to a higher water table.
Furthermore, as can be seen in Figures 4.6a and 4.6b, the magnitude of the meltwater events increases in both scenarios. An increased seasonal amplitude in meltwater input, due to higher peaks in the melt season, caused by higher temperatures and more rain-on-snow events, causes a stronger water table height reaction. These effects combined might explain the increase in variability with time: higher density means a higher water table response from meltwater input, and more meltwater input in every melt season causes the water table to rise faster during melt seasons in the future than it did in the past, causing the intra-annual variability to increase. Thirdly, a higher density means that the hydraulic conductivity decreases, making it harder
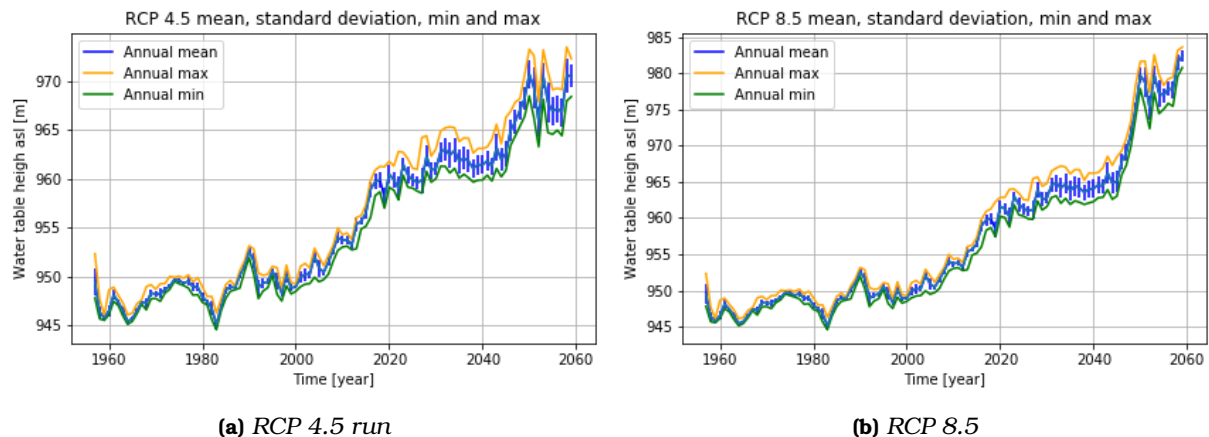
(a) *RCP 4.5 run* **(b)** *RCP 8.5*

Figure 6.5: *Annual and spatial mean (blue line), standard deviation of the mean (blue bar), maximum (orange) and minimum (green) water table for all three model experiments.*

for water to flow. This means that water needs to pile up more to achieve the same amount of discharge per cell, a higher head gradient is needed to obtain a new equilibrium, and therefore this causes the water table to rise.

We found in this study that the PFA on the Lomonosovfonna needs to be present in 1957 for the model to produce water table heights closest to observations in 2017. It is therefore likely that the accumulation rate isolated the PFA from the cold wave from the surface temperature, making it possible for the PFA to persist and grow. The notion that the PFA was already present in 1957 is supported by Figure 6.3. Just after 1957, the temperature climate regime retrieved from observations shows a temporal dip, which is also visible in the annual and spatial mean of the modelled head height, see Figure 6.5. In the beginning of the 70's, the temperature regime goes up, but still remains a little below the temperature regime present in the period 1920 - 1960. Since the water table height is increasing slightly in the period 1970 - 2000, and the temperature regime in 1920 - 1960 is warmer compared with the period 1970 - 2000, it can reasonably expected that the aquifer was already present before 1957, since a warmer climate favours PFA formation.

In Figures 6.6a and 6.6b, the total water table height change over the period 1957 - 2060 per grid point is shown, for both RCP scenarios. This is done by taking the average water height in the first year of the historical run, and subtracting it from the average water table height of the last year. The surface height, which was taken as constant during the model runs, is presented in Figure 6.7.

In general, areas with a lower surface elevation experience a bigger increase in water table height compared with cells with a higher surface area. The RCP 8.5 shows a higher trend compared with the RCP 4.5 scenario. It can also be seen that around two local peaks in the southwestern part of the grid, indicated by two white stars, the increase is larger than in the rest of the grid, while the peak itself experiences a small water table height increase. This is more pronounced in the RCP 8.5 scenario. Most likely this is because the water flow follows the elevation profile of the model, which was also found by Hawrylak and Nilsson (2019). Large height differences mean large flows, and if cells get saturated in the lower parts of the model, water will start to pile up at places upstream. Water seems to pile up at places where the surface elevation lines are close together, so where the surface gradient is large.

(a) *RCP 4.5 run*   **(b)** *RCP 8.5*

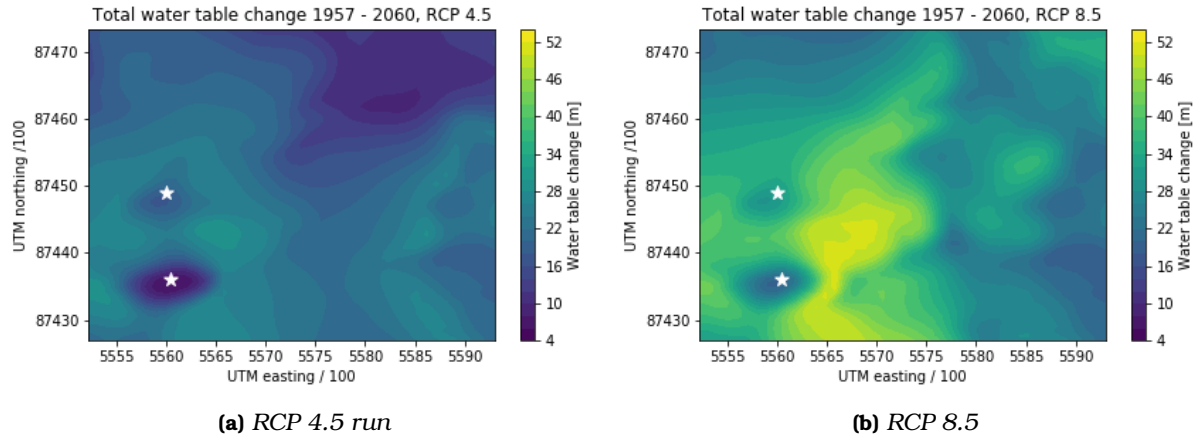**Figure 6.6:** *Total water table height change 1957-2060 for the RCP 4.5 scenario (Figure 6.6a) and the RCP 8.5 scenario (Figure 6.6b). White stars indicate local peaks in the surface elevation, see Figure 6.7*
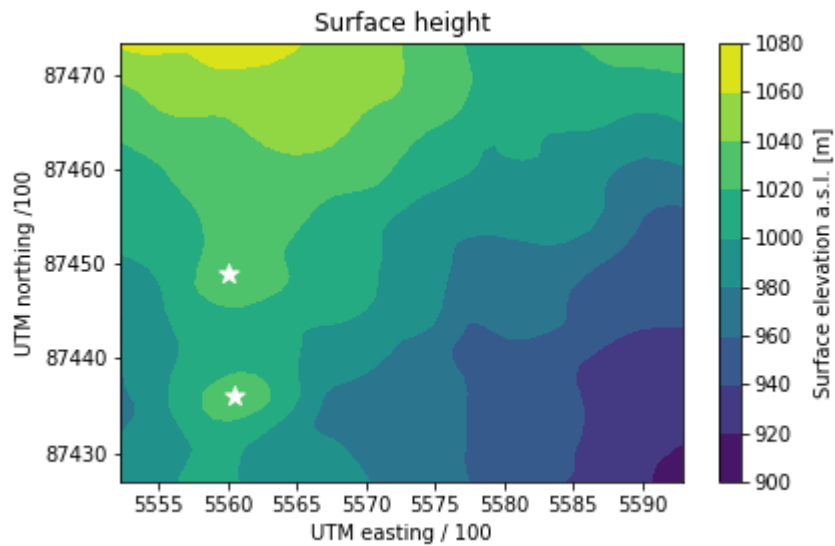

Figure 6.7: *Surface elevation above sea level in the modelled grid, repeated from Figure 3.2. White stars indicate local peaks that experience remarkably small water table height increases, see Figures 6.6a and 6.6b*

Figure 6.8 shows per timestep the percentage of the surface cells in which the water table height exceeds the surface, referred to as 'surface events'. This did not happen in the historical run. In the RCP 4.5 scenario, the first surface event happens around 2048. In the RCP 8.5 scenario, the first surface event happens around 2048. From 2049 onwards, the percentage of cells with surface events in the RCP 8.5 scenario stays above zero, indicating that water will stay at the surface even during winters, the surface events can be from then regarded as perennial. There are timesteps after 2050 in the RCP 4.5 scenario where the water table does not reach the surface anymore. There are three sharp increases in the amount of surface events visible in both scenarios: around 2050, around 2053 and around 2058, coinciding with peaks in the water table height shown in Figure 6.5a and 6.5b. In both scenarios there are peaks in the average density around these years, as can be seen in Figure 4.5a and 4.5b. There is a seasonal pattern, but the number of cells is obviously increasing. The counts per grid cell, summed over the simulation period are presented in 6.9, showing that all surface reaching events happen in the eastern part of the model, where also regularly the modelled values are overestimated, as shown in the model tuning experiments.
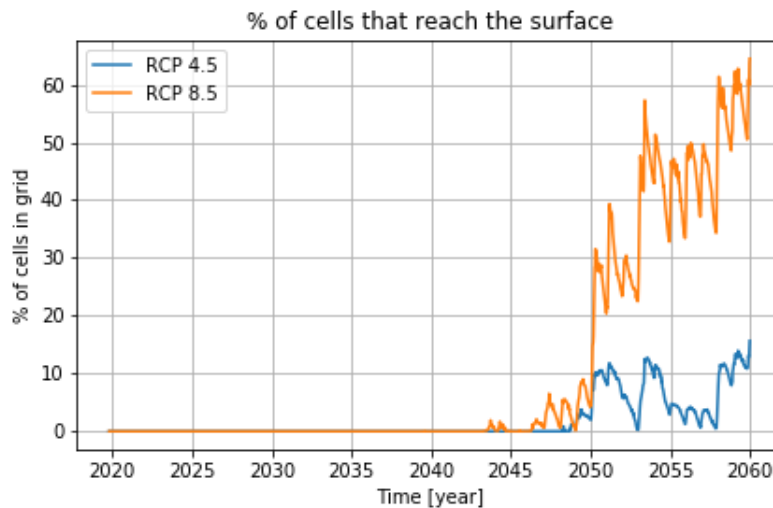
Figure 6.8: *Percentage of surface cells with a water table that exceeds the surface*

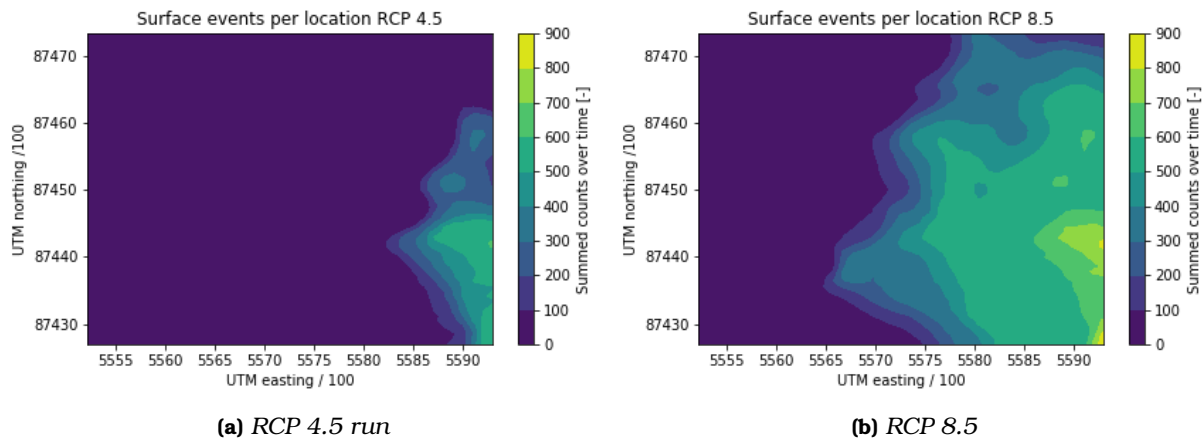**(a)** *RCP 4.5 run*   **(b)** *RCP 8.5*

Figure 6.9: *Counts of surface events per surface grid cell over the full run (2135 timesteps) for both the RCP 4.5 and RCP 8.5 scenario*

The surface height of the model grid is shown in Figure 6.7. From the patterns shown in chapter 5, it can clearly be seen that the local peaks in the south western part of the model, marked with the white stars, has a low head height. They are on all sides surrounded by terrain with a lower elevation, and therefore, water will disperse away from the peaks. Water seems to pile up on the eastern side of the grid, coinciding with what seems to be a small outlet valley with lower surface elevations.

6.3 Water table height versus meltwater input - temporal case study

In Figures 6.10 the modelled water table height is shown in combination with the meltwater input for a specific period in the historical and future run (RCP 4.5). As can be seen, the water table height matches the pattern of meltwater input: almost immediately after the meltwater input peaks, the modelled water table height peaks as well. The high meltwater peak in 1998 in the historical run (Figure 6.10a), causes a significant water table height increase. The modelled PFA appears to take three years to 'recover' from that event. This can also be seen in the future runs: after a meltwater input peak in 2045, the water table recovers over the rest of the year, but does not go down to the water table height of before the 2045 meltwater input peak: the next meltwater input peak of 2046 happens already and the water table rises accordingly, causing the water table to increase with time.

High meltwater input peaks are rare in the historical run, the 200 mm/week event in 1998 is the highest in the dataset (see Figures 4.6a and 4.6b), 100 mm/week can already be considered as a 'high meltwater input event' in the historical run. There are sequences of 5 years where all meltwater events are below 50 mm/week. In both future runs, meltwater input events of 100 mm/week are common, in the final years of the future runs the meltwater input does not drop below 100 mm/week. The peaks are also slightly broader, as can be observed in Figure 6.10b, which is because the melt seasons in the future scenarios are longer than in the past, and provide therefore more water to the aquifer.

(a) *Historical run (1957 - 2019)*   **(b)** *RCP 4.5 (2019 - 2060)*
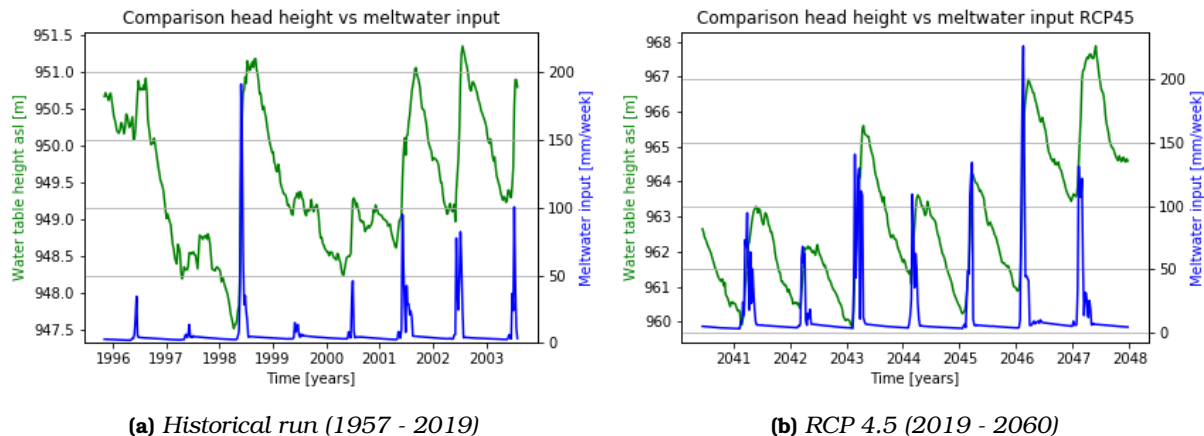
Figure 6.10: *Water table height asl (green, left y-axis, note the different scale between the historical and future temporal case) compared with meltwater input (blue, right y-axis), for a small sequence of the full run in the historical and RCP 4.5 experiments*

To get a rough estimation on how fast the water table lowers after a meltwater event, the local peaks and minimums were determined. Then, the difference in head height between a peak and a subsequent minimum is divided by the time difference between them to get a linear ap-

proximation of the head height decrease rate after a meltwater input event. The peaks identified in the temporal case studies presented in Figure 6.10, is presented in Figure 6.11.

(a) *Historical run (1957 - 2019)*   **(b)** *RCP 4.5 (2019 - 2060)*
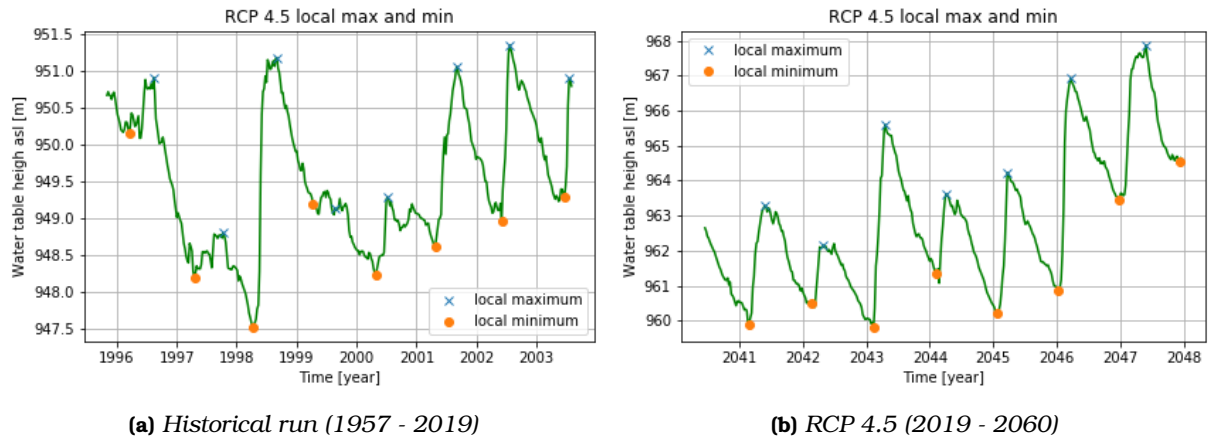
Figure 6.11: *Peaks and minima used to compute the average linear head height decrease*

The average head height decrease rate in the RCP 4.5 temporal case study is 8.6 cm week^{-1}, in the historical temporal case study 4.9 cm week^{-1}. Although the density is larger in the RCP 4.5 scenario compared to the historical run, and therefore the hydraulic conductivity is lower which causes the flow between cells to be lower, the average head declines faster in the RCP 4.5 scenario. A higher density also means less pore space, less pore space means that there can be less water stored in cells and that the water table height will be effected more by in- and outflow. This in combination with larger meltwater input fluxes likely cause the head height decrease between meltwater input events to be larger in the future scenario.

The distance between a peak and minimum in the future scenario is ±45 weeks. In 45 weeks, given the average head height decrease rate, the water table will lower with 3.9 meters. The relative smaller peaks in the years 2040 - 2043 of the temporal case of RCP 4.5 cause a water table height increase of 3.1 meters and less, and it can be seen in Figure 6.10 that the water table (almost) recovers fully to the level before the peak before the next meltwater event happens. The peak caused by a strong meltwater event in 2043 is ±5 meters, and the water table height does not fully recover before the next meltwater event happens. This is also the case for the peaks in the period 2046 - 2048. In the historical scenario, the average distance between a peak and a minimum is ±50 weeks, and in 50 weeks the water table lowers on average with 2.45 meters, causing the meltwater input events that cause a water table increase of more than 2.45 meters (1998, 2001-2003) to raise the average water table height, which is the case for 1998, 2001 and 2002.

Because the flow between cells is dependent on the head height difference, the water table height decrease rate is expected to depend on the water table height itself. This would suggest that the water table height decrease over time is a simple differential equation, and it should follow an exponential decrease curve. However, no fitting exponential curve could be found for the water table decrease events in both scenarios (using a least-square method and Python's `scipy.optimalize.curve_fit`), pointing out that, at least right after a meltwater input event, the water table decrease does not follow an exponential curve.

6.4 Flow characteristics

The flows calculated by MODFLOW 6 were saved and processed to obtain their magnitude (m^3 week^{-1}) and direction. The results are presented in this paragraph.

The normalized flow vectors plotted over the surface elevation profile for all three model experiments are shown in Figure 6.12. The average flow magnitude for all three model experiments is plotted in Figure 6.13. Apart from a circular-like pattern around the two local peaks, the flow pattern generally follows the elevation lines, which was also found by Hawrylak and Nilsson (2019). There is a small area in the northwestern part of the model grid where for all three model experiments the average flow direction is uphill. Given the fact that average flow magnitudes in that area are very small compared to the rest of the grid (see Figure 6.13), so this is regarded as incidents caused by local effects. It can also be the effect of the boundary effects. The bufferzone and boundary conditions tests were done with the water table height as precursor, no sensitivity tests of the boundary conditions on the flow patterns were conducted.

In all scenarios, the average flow direction is to the south-east, and flow magnitudes are largest in the southeastern part of the model grid. This area looks on the surface elevation profile like a small outlet glacier, see Figure 6.7, and seems to act as the main path for water to leave the model grid.

The annual mean-, maximum- and minimum flow are shown Figure 6.14. Just as with the water table heights, the variability in the historical run is much lower than in both future scenarios. There is however a multi-annual cycle visible in the annual average flow of the historical run. The same graph for a run with constant density is presented in Figure 6.15, where there is much less of a cycle visible in the historical run, leading to the conclusion that density changes cause the multi-annual cycle shown in Figure 6.14 for the historical run.

Average horizontal flow speeds increased in both scenarios, as well as the variability, compared to the historical run. This is equivalent to the water table heights: if the head height becomes more variable, the flows will follow and if the flows become more variable, the head height will follow. Since meltwater input is first added per column, first the head height increases, and then the flows will be calculated. So the variability in the flows follows from a variability in the head height, which is a reaction to the increased density and meltwater input.
Density is used to calculate the hydraulic conductivity, and therefore directly influences the flow magnitude. The experiment was repeated with a constant density, see Figures 6.15a and 6.15b, and the fluctuations almost disappear. Also, in the case of a constant density, the final flow magnitude is larger in both scenarios, and the RCP 8.5 has larger flows compared to RCP 4.5. Making the density time-dependent therefore has two effects: it enhances the fluctuations in flow magnitude and it decreases the flow magnitude in both scenarios.

Since the flow, porosity and water table height are known, the average residence time per column could be calculated, using Equation 6.1, in which t_{res} is the residence time per column, the V_{column} the volume of water in the column, $P(z)$ the porosity, $delr$ and $delc$ respectively the width and the length of a column and h the head height.The resulting average residence time per column can be seen in Figure 6.16a.

$$t_{res} = \frac{V_{column}}{\sum Flow_{column}} = \frac{P(z) * delr * delc * h}{\sum Flow_{column}} \tag{6.1}$$

In the historical run there is again a multi-year cycle visible, that is opposite to the cycle seen in the flow magnitudes (see Figure 6.13). This is expected: large flow magnitudes cause small

(a) *Historical run*

(b) *RCP 4.5 run*

(c) *RCP 8.5*
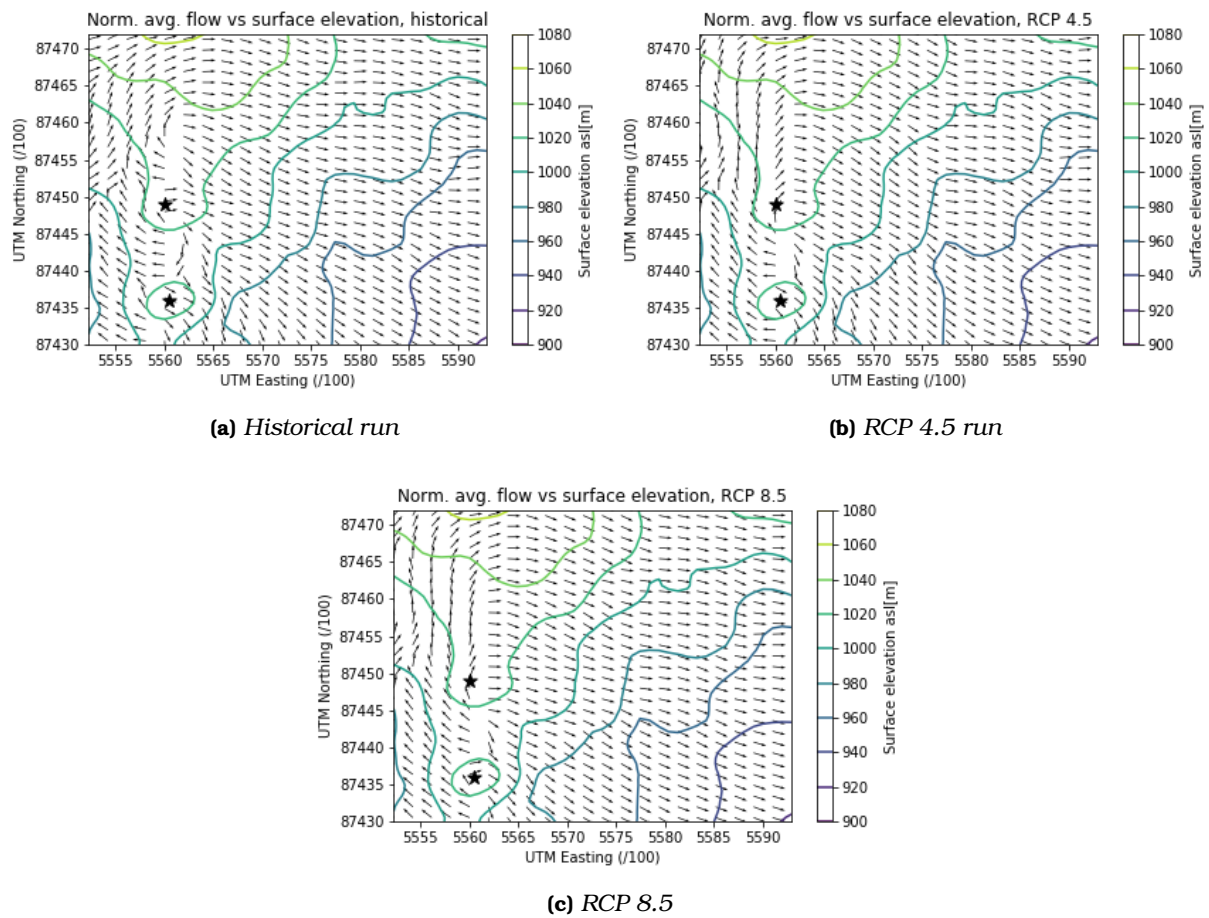
Figure 6.12: *Time-average normalized flow vectors plotted over the surface height contour lines. The resolution has been lowered by a factor 4 to increase the readability of the vector arrows. The black stars correspond to local peaks, as shown in Figure 6.7*

(a) *Historical run*

(b) *RCP 4.5 run*

(c) *RCP 8.5*
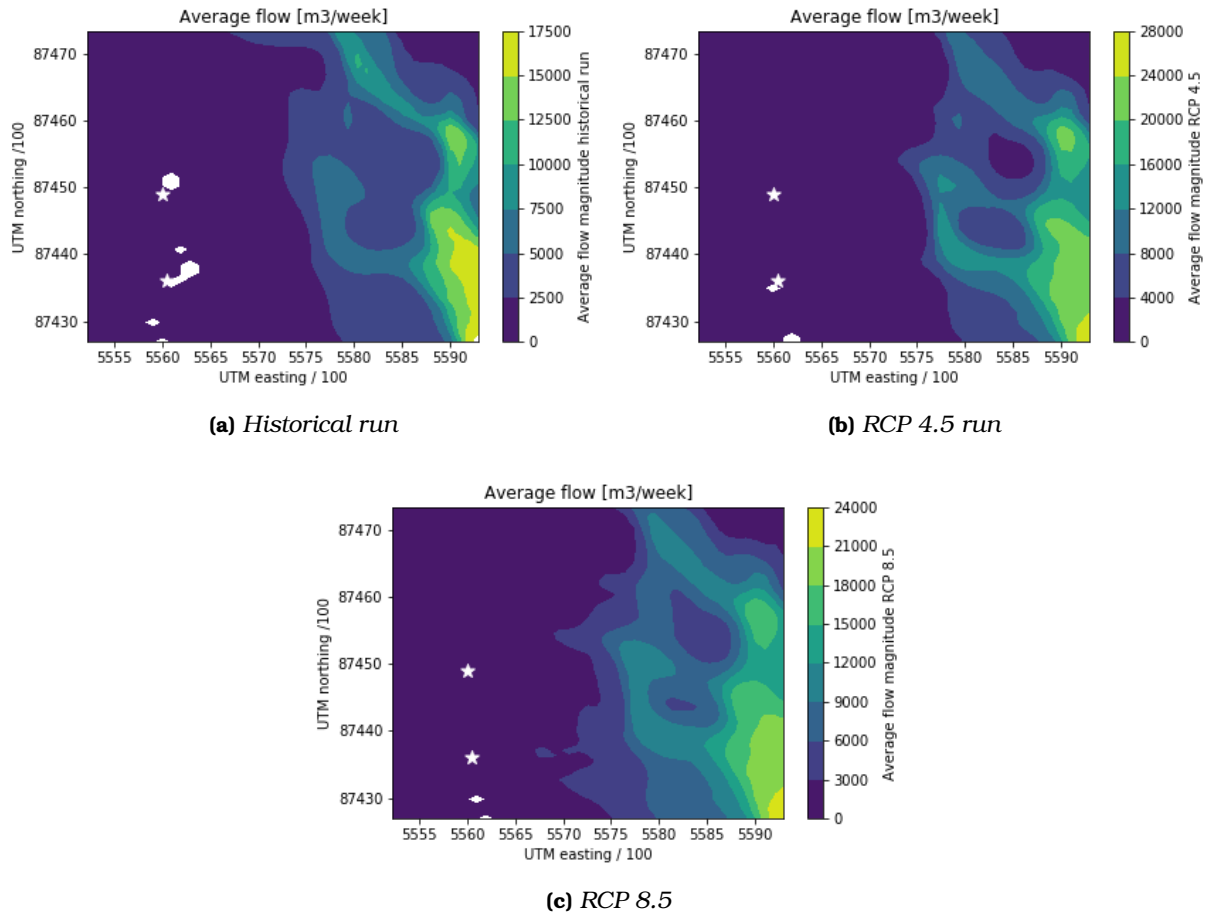
Figure 6.13: *Time-average flow magnitude for all three model experiments The white stars correspond to local peaks, as shown in Figure 6.7. White spots apart from the stars are areas where the flow magnitude is so close to zero, that Python could not the average flow vector.*

(a) *RCP 4.5 run*

(b) *RCP 8.5*
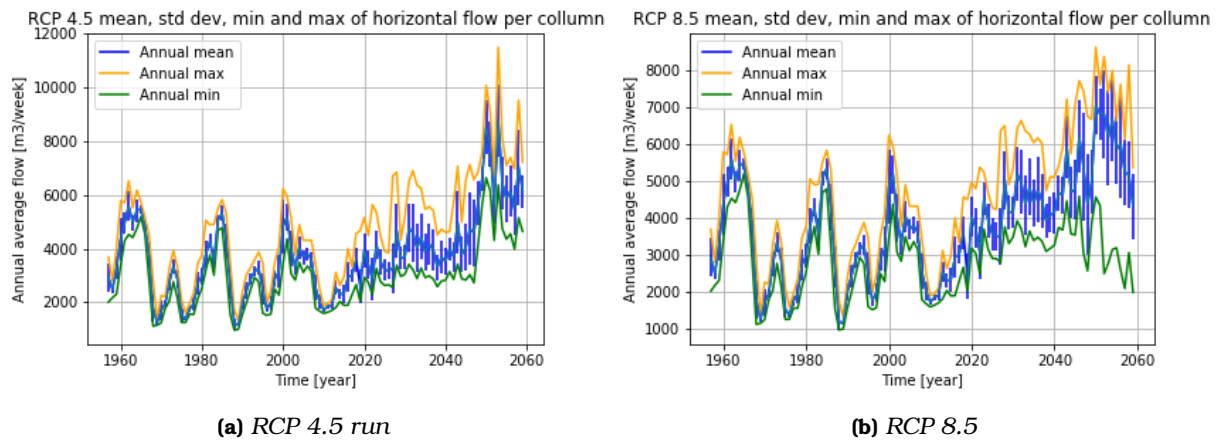
Figure 6.14: *Annual mean, standard deviation of the mean, maximum and minimum flow for all three model experiments.*

(a) *RCP 4.5 run*　　　　　　　　　　　　　　　　**(b)** *RCP 8.5*
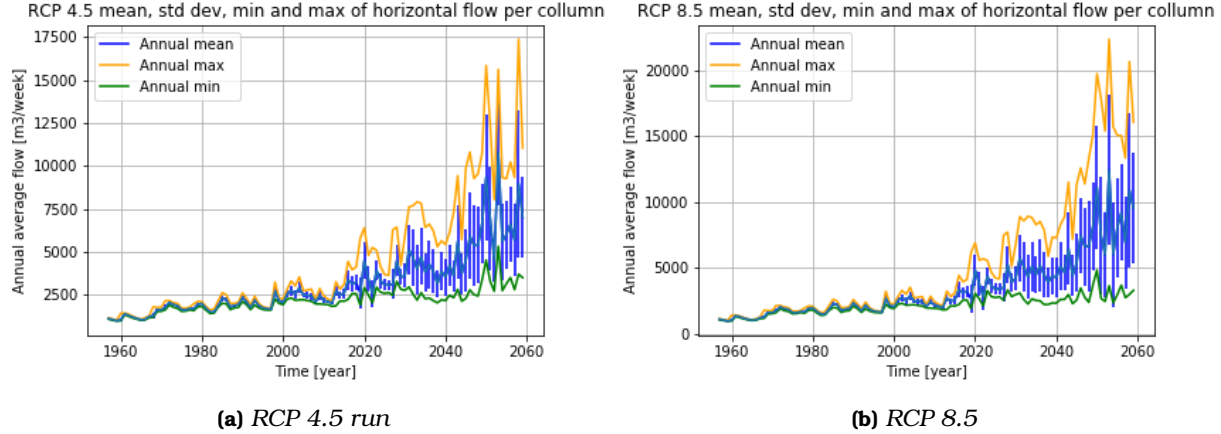
Figure 6.15: *Annual mean, standard deviation of the mean, maximum and minimum flow for all three model experiments with a hydraulic conductivity that is calculated with the average density of the 1957 - 2019 data set, and then kept constant during the whole simulation.*

residence times according to Equation 6.1. For both future scenarios, the residence time per column decreases, which is likely because flow magnitudes rise, and the water volume decreases due to decrease in porosity, which is in turn caused by an increase in density. Around 2040, in the RCP 4.5 scenario, the residence time is slightly higher than in the RCP 8.5 scenario. This coincides with a small drop in the water table height (see Figure 6.5a). The drop in water table height is not visible in the RCP 8.5 scenario, see Figure 6.5b. Also, unlike the flow magnitude and water table heights, there is not much difference in mean residence time between both RCP scenarios.

The lack of difference between the RCP 4.5 scenario and RCP 8.5 scenario in mean residence times is likely caused by a combined effect of larger flow magnitudes and a larger volume of water present per column. According to Eq. 6.1, if the flow magnitudes increase, the water volume per column should increase as well to keep the residence time equal. The flow magnitudes are larger in the RCP 8.5 scenario compared to the RCP 4.5 scenario, so the volume of water in the RCP 8.5 scenario should be larger as well. The average water content per column per time step is shown in Figure 6.16b, in which is indeed visible that the RCP 8.5 scenario on average has a larger water content per column compared to the RCP 4.5 scenario. The water content is determined by the water table height and the porosity. Although the average density is higher in the RCP 8.5 scenario, and therefore the porosity is lower, the average water content per column is still larger compared to the RCP 4.5 scenario, thereby implying that the increased water table height has a larger effect on the total water content than the decreased porosity.

The temporal averaged residence times per column per model experiment are presented in Figure 6.17. Generally, areas with a higher surface elevation have a larger residence time, with extreme values outside of the range presented in Figure 6.17, which is likely caused by the low flow magnitudes in these areas. The residence times at the regions with a higher surface elevation, in the western part of the model grid, increase in both future scenarios. This is likely caused by the increase in density. Water in these spots is present in the lower layers of the LPFAM, layers that have a high density. An increase in density in those layers will have a larger effect on the hydraulic conductivity than in the upper layers, and therefore on the flow magnitudes, because the slope of the density-hydraulic conductivity function decreases for higher densities. The channel-like pattern observed in the eastern part of the grid generally coincides with the channel-like pattern seen in the average flow per column in Figure 6.13.

(a) *Mean residence time per column*

(b) *RCP 8.5*
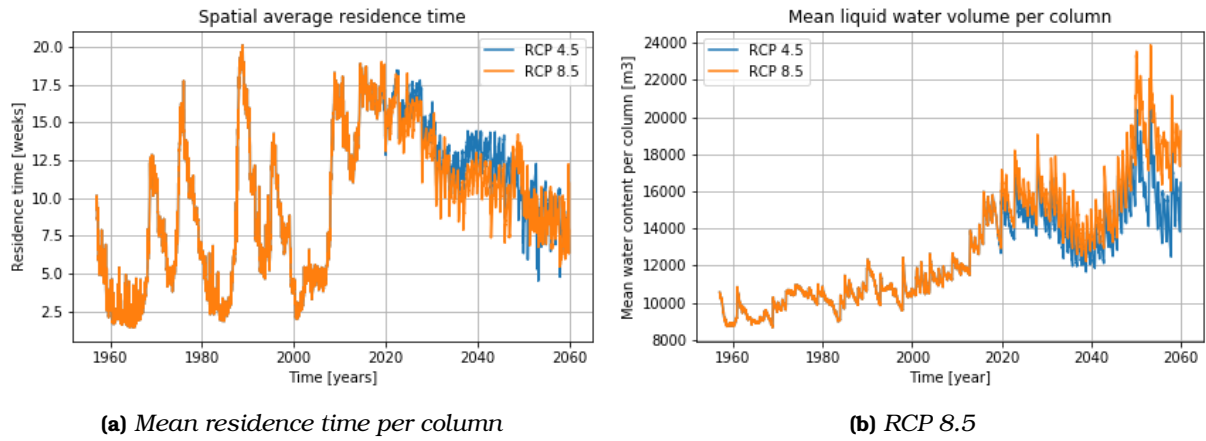
Figure 6.16: *Figure 6.16a: Residence time per column for 1957 - 2060 for both RCP scenarios. Figure 6.16b: Average water content per column for both RCP scenario's. The total volume of one model column is ±345000 m^3.*

(a) *Historical run*

(b) *RCP 4.5 run*

(c) *RCP 8.5*
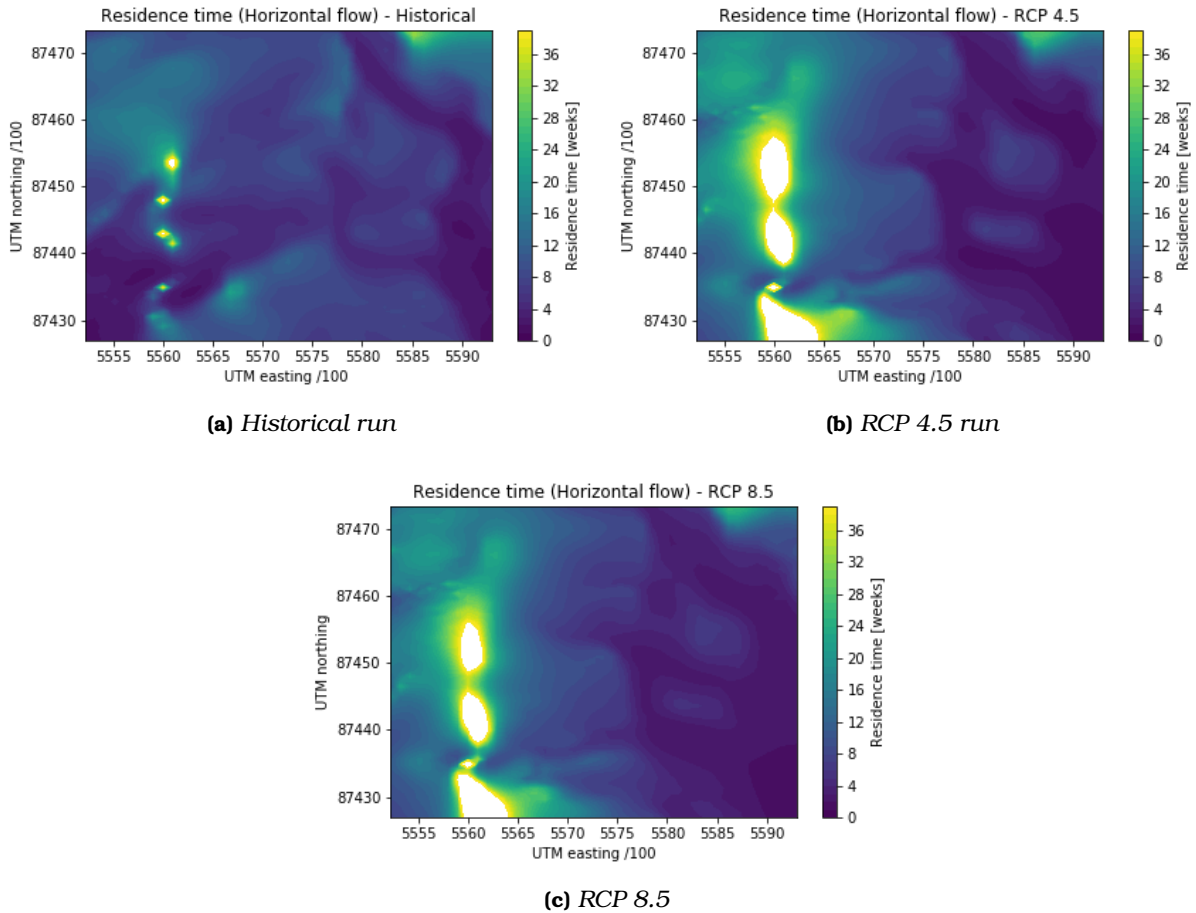
Figure 6.17: *Time-average residence times for all three model experiments. White spots are areas where the flow magnitude is too large for the pot value extent, this is done to make the patterns in the eastern side of the model grid visible.*

6.5 Correlation between time series

The output of the LPFAM consists of two time series: grid averaged water table height and grid averaged flow magnitude. The density and meltwater input from the EBFM is a time series as well. First, the annual average of all values was calculated, to get rid of the seasonal cycle. Then, Pearson's R was determined. The resulting correlation coefficients can be observed in Table 6.1, 6.2.

Table 6.1: *Correlation coefficients between timeseries in the historical run (1957 - 2019)*

Pearson's R HIS	Water table height	Flow magnitude	Density	Meltwater input
Water table height	1	-0.33	0.35	0.60
Flow magnitude	-0.33	1	0.055	-0.07
Density	0.35	0.055	1	0.55
Meltwater input	0.60	-0.07	0.55	1

Table 6.2: *Correlation coefficients for RCP 4.5 (bold and underlined, bottom left) & RCP 8.5 (normal text, upper right) for 2019 - 2060.*

Pearson's R RCP 4.5 & 8.5	Water table height	Flow magnitude	Density	Meltwater input
Water table height	XXX	0.96	0.9	0.77
Flow magnitude	**0.96**	XXX	0.63	0.54
Density	**0.87**	**0.83**	XXX	0.79
Meltwater input	**0.77**	**0.75**	**0.68**	XXX

The correlation coefficients in the historical run are low compared to the correlation coefficients in the future runs. This could be because input data in the historical scenario consist of downscaled observations, which contain possibly noise. The future runs consists of datasets that are made with the variability of the years 1989 - 2019, but some noise will be lost in the projection process. Especially the flow magnitude - density correlation coefficient is low, since the hydraulic conductivity is directly dependent on the density. This is likely because the density is lower in the historical scenarios, and for lower densities the hydraulic conductivity-density function is almost flat.

The best-fitting hydraulic conductivity was found to be a cubic distribution, with an increasing slope as depth increases. The maximum hydraulic conductivity in this distribution is slightly above 1300 m week^{-1} for low densities, and the minimum is 15.12 m week^{-1} for high densities of the firn. The minimum value is in line with what is found in literature, because it was fixed at that value for high densities, but the maximum value is more than twice as high as values found in the literature. This could mean that the hydraulic conductivity is compensating for physical processes that are not part of the model, to fit with the observations. This could be the effect of uncertainties in the density from the EBFM model, if the EBFM model overestimates the density of the firn, there will be less pore spaces available to store water in and the water table will rise faster. Overestimation of the density can also be the effect of the layer-picking from the 75 layers in the EBFM to 5 layers in the LPFAM. For every fifteenth EBFM layer, the depth-coordinate is chosen as bottom of the corresponding LPFAM layer, and the density is used for the full LPFAM layer above it. This is done to ensure that the LPFAM has the same vertical extent as the EBFM, but by doing so, the LPFAM likely uses an overestimated density, because the density at the bottom of a layer is used as density for the full layer above it. As alternative, one could use the average depth and density of the EBFM over fifteen layers for one LPFAM model layer, but this will decrease the vertical extent of the LPFAM from ±55 to ±38 meters.

A high hydraulic conductivity will cause larger flow magnitudes and therefore a faster decrease in head height, counteracting the overshooting density. Also, in this model all pore spaces below the water table are assumed to be filled, which might not be the case, especially for high densities. If not all pore spaces are filled, the water content per cell will be lower, so to compensate for a higher water content per cell, a higher hydraulic conductivity is needed to ensure the same increase and decrease in water table height.

The model underestimates the water table in the western part of the model grid. This could be the effect of the full pore space saturation assumption. On large depths, where densities are close the density of ice, pore spaces might not be connected anymore, and therefore water cannot flow there, meaning that water will pile up on this layer. If this is added to the model, the water table in the lowest layer will rise, which will likely make the modelled water table in the western part of the model closer to the observations.

The modelled water table heights in the eastern part of the model grid are an overestimation compared to the observations. Adding a crevasse in that region decreased the best fit hydraulic conductivity, its RMSE, and the errors in that area. From this can be concluded that the lack of sinks in the model grid, in this test case a crevasse, is likely compensated by a high hydraulic conductivity in the upper LPFAM layers. A higher hydraulic conductivity namely will make the water flow away easier, a lower hydraulic conductivity will make water pile up faster. A sink drains water from the model grid, therefore requiring a lower hydraulic conductivity to obtain the same water table heights.

In the eastern part of the model grid, where the overestimation of the water table happens, the modelled water table depth is around 10 meters or lower, it will get close to the surface. From 0-10 meters below the surface, one could expect that the PFA will not be fully isolated anymore from the low surface temperature during the winter, and less water in the PFA will refreeze. Refreezing acts as a sink and takes away water from the PFA, making it part of the firn package, effectively lowering the water table. Refreezing is not part of the LPFAM, and a higher hydraulic conductivity causes larger flows and might therefore compensate for the missing refreezing sink.

The LPFAM did not produce water table heights close to observation when the initial conditions in 1957 were set to be empty, suggesting that, according to this model study, the perennial firn aquifer has been present since 1957 and likely longer before that. This is confirmed by the climate data from Longyearbyen airport (see Figure 6.3), the period before 1957 (1920-1957) was warmer than the first years of the LPFAM model runs (1960 -1970), and slightly warmer than the following years in the historical runs (1970-2000). A warmer climate on Svalbard favours the formation of an aquifer, more meltwater will be available and refreezing during winter will be less. In this model study we found that the PFA persists and even grows slightly in the period 1960-2000, if the PFA could persist and grow in that period with a relative cold climate, it is very likely that it could persist and grow from 1920 - 1957 as well.

As found in the model study of a PFA on the Greenland Ice Sheet by Kuipers-Munneke et al. (2014), high accumulation and high melt rates are favourable for perennial firn aquifer formation. This is needed to protect the aquifer from refreezing, and to ensure enough water input to balance outflow and refreezing. The Lomonosovfonna has high accumulation rates, 1.2 - 1.8 m.w.e a^{-1}, and Kuipers-Munneke et al. (2014) mention a accumulation rate of 1.75 m.w.e. a^{-1} as being large enough to isolate the percolating water to become perennial but too small to provide enough cold content to fully refreeze. The conditions on the Lomonosovfonna ice cap are comparable to the conditions on the test sites of Kuipers-Munneke et al. (2014) on the GrIS, see Figure 6.2. Therefore, this model study shows that the range on accumulation rates of Kuipers-Munneke et al. (2014) applied to the GrIS, likely is similar for perennial firn aquifer formation on Svalbard.

The average modelled water table rose in the historical run (1957 - 2019) with 10 metres, and with 12.5 and 20 meters for RCP scenario 4.5 and 8.5 respectively. The water table rise in the historical scenario and the RCP 4.5 scenario, 16 cm a^{-1} and 30 cm a^{-1} respectively, are in the range presented by Miller et al. (2020) (9 - 30 cm a^{-1}), obtained from measurements on the GrIS. The rise of the water table in the RCP 8.5 scenario is with 49 cm a^{-1} outside the range. The water table height correlates in both scenarios with the meltwater input, and the meltwater input is in general larger in the RCP 8.5 scenario
The first surface events happen in 2044 for the RCP 8.5 scenario and in 2048 in the RCP 4.5 scenario. Around 2046 (RCP 8.5) and 2050 (RCP 4.5), the model predicts water table heights above the surface for multiple consecutive years. After that, the occurrences of these events increased. At the end of the simulation, almost 60% of the surface cells in the RCP 8.5 scenario contained a water table at the surface. The density increase and the increase in meltwater input in the RCP 8.5 likely are the cause of this: higher density makes water pile up easier because of a higher hydraulic conductivity and less pore space, making the PFA rise faster for a given meltwater input. There are no processes related to refreezing and ice lense formation modelled in the LPFAM, see Table 4.2. Both processes are expected to happen in the upper layers during the cold season, and both processes will lower the water table height, thereby reducing the increase of the water table close to the surface. This makes the results from this model study for both future runs likely an overestimation: if refreezing and ice lens formation are part of the model, the modelled head height increase will likely be lower and it will likely take the water table longer to reach the surface. The water table did not reach the surface in the historical scenario, so this does not apply for those results.

The seasonal amplitude in water table height increased in both future scenarios compared with the historical run. It is likely that the variability is to a large extent due to the growing density: a higher density means less pore space available, making the aquifer respond more to meltwater input. Also, the meltwater input increases in the future scenarios. These effects combined make the peak in the water table after the melt season higher compared to the historical run. Both meltwater input increase and firn densification follow from the RCP scenarios: more meltwater input is because surface temperatures increase, and more meltwater percolation means more

refreezing and lower accumulation, and therefore a higher density. Precipitation in general and rain-on-snow events are expected to increase on Svalbard for both RCP scenarios (Osuch and Wawrzyniak, 2016), causing more gravitational densification in winter and more water input in summer, but also a thicker layer with fresh snow and a lower density on top of the firn package, sheltering the PFA more during the cold season.

The EBFM tracks water fully down until ice layers are reached, taking refreezing and water lost as irreducible water content into account, because there is no aquifer modelled. However, in the LPFAM, the water flux from the EBFM is directly added to the top of the aquifer. Since the water flux passed through all layers in the EBFM, but is added at a smaller depth in the LPFAM, it is likely that the meltwater input at the water table of the PFA is an underestimation, since it passed through more layers in the EBFM and has therefore experienced more refreezing and loss due to irreducible water content than it would have if the water only percolated to the water table depth in the LPFAM.

The average residence time per column decreased in both RCP scenarios, likely because an increase in the flow magnitude, and a less pronounced increase in the liquid water content. There seems to be a stabilization of the residence times around 2040, where for a few years the average residence time per column for the RCP 4.5 scenario is larger than for the RCP 8.5 scenario. This coincides with a period of stable water table heights (see Figure 6.5), and with a dip in the average volume of water per column (see Figure 6.16). Apparently, an equilibrium is reached in that period, the water table is high enough to reach layers with a high hydraulic conductivity, therefore the flows are getting larger and the head height rise stabilizes. Also, the magnitude of the meltwater input events around 2040 are low for both future scenarios (see Figures 4.6a and 4.6b), and the density reaches a local minimum around 2040 for both scenarios, following a peak around 2035 (see Figures 4.5a and 4.5b). A lowering density will have a double negative effect on the water table height: a lower density will cause a higher hydraulic conductivity, which makes water flow away more easily, and creates more pore space for water to be stored in. The higher hydraulic conductivity in combination with the low meltwater input events around 2040 likely cause the dip in liquid water volume per column, with a lower average density in the RCP 4.5 and therefore a lower average water content per column in that scenario.

Residence times are shorter in the eastern side of the model grid, following roughly the surface elevations.The average flow direction is similar for all three model runs, and is approximately east-south-east, towards the lower elevations of the model grid, see Figure 6.12a, 6.12b and 6.12c. The most surface breaching events happen as well in the eastern part of the model. Hawrylak and Nilsson (2019) found a similar south-eastern trend in head height gradients from the measurements at the Lomonosovfonna ice field.
It is expected that, just outside the model grid at the south-eastern part, there exist a crevasse field that may act as a sink for the PFA. There is no data available on the crevasse, so there is no proof that they are present. However, crevasses might explain the overestimation of the water table height in that part of the model grid. The first and most surface reaching events happen in that part of the model, and the average flow direction is towards it. Also, during the tuning process, it was evident that the model produced a water table to close to the surface compared with observations in the south-eastern area of the model grid.

The equilibrium line altitude (ELA) is near the Lomonosovfonna estimated at 719 m a.s.l. (van Pelt et al., 2012). Hanssen-Bauer et al. (2019) mention an average increase of the ELA of 400 meters between the periods 1971- 2000 and 2071-2100. The lowest elevation in the modelled grid is ±900 m a.s.l. and in the bufferzone ±750 m a.s.l. It is therefore likely that during the future runs of the LPFAM, parts of the surface of the bufferzone and model grid will be below the ELA, meaning that there will be effectively mass lost. In the most extreme case, this could mean that places with a surface elevation below the ELA, the total firn layer disappears, making

it impossible for a PFA to persist, and its water could runoff instantly.

7.1 Limitations

The most important limitation of this research is that there are no interactions modelled between the PFA and the firn layers. If the PFA is far beneath the surface, this might be a justified assumption, because firn characteristics (such as temperature and density) are almost constant there. But temperature starts to vary closer to the surface, it follows the surface temperature. This means that during the winter, the firn close to the surface at the Lomonosovfonna can reach temperatures of -20 to -30 °C. If there is water present in these upper firn layers, which there is in the future scenarios according to the results presented here, it could be reasonably expected that a large portion of this water will freeze and become part of the firn, therefore increase its density. Horizontal plates of ice, referred to as ice lenses could be formed as well, they might block melt water input in the next melt seasons from entering the aquifer. The blocked water will then persist on the ice lens, where it will freeze during the next cold season, thereby increasing its thickness, or it can runoff to lower elevations. Refreezing of the percolating water is part of the EBFM, but once the water becomes part of the PFA, refreezing is not taken into account. Since ice-firn interactions such as refreezing and ice lens formation decrease the amount of water present in the firn aquifer, adding these processes in the model would likely lead to a decrease in modelled water table heights.

Future research can use this model to achieve a two-way coupling with an existing firn-model, such as the EBFM, to make connections between the PFA and the firn possible. This can be in the subsurface, for example by adding exchanges in energy between the aquifer and the firn, thereby altering the thermodynamic profile of the firn. Refreezing can be added subsequently, to let aquifer water refreeze and become part of the firn layers, increasing the density and temperature of the surrounding firn. Furthermore, if a surface routine is developed to handle water table heights that exceed the surface, this could be added to the surface energy balance in the EBFM. Surface streams and lakes have a higher albedo than the surrounding snow, creating dark spots on the ice cap with a different energy balance compared to the surrounding snow.

Recharge in the LPFAM is directly added to the top of the PFA, because the percolation is already part of the EBFM. The first step to connect the models could for example be adding the percolation process, including refreezing and compaction of the firn column, to the LPFAM. The vertical firn model developed by Kuipers-Munneke et al. (2014) could be used as example.

When water reaches the surface and rises above it in the LPFAM, the water table is set back to the surface, discarding all the water that is above it. This is obviously not what happens on the ice field. MODFLOW 6 has packages to simulate lake formation and to simulate surface streams. However, streamflow routing requires input data like surface roughness and probable paths the surface flows will take. At present it is not possible to prescribe these for the Lomonsovfonna ice cap, but future modelling attempts in combination with more data on surface conditions on the Lomonsovfonna, for example obtained from field campaigns or remote sensing, could be used to add a fitting surface routine to the LPFAM.

A lot of processes not included in the LPFAM, such as the formation of ice lenses and surface routing, require data in order for them to add to the model. Ice lens formation can be studied by controlled experiments in a firn column in a laboratory, but they can also be detected using the same GPR-method used to obtain water table depths. If there is spatial data available on the location, size and temporal variation in ice lenses, it can be combined to formulate a statistical description of ice lens formation, that can be added to the LPFAM. Crevasses can

be detected during field work campaigns, but probably also by using airborne data such as photo's, or even with radar surveys. Surface characteristics used to model surface routing if water reaches it, such as the hydraulic conductivity of the surface and local 'riverbeds' (areas with local lower elevations, where water can easily discharge), can probably also be determined by surface images. Also, the surface elevation is kept temporally constant, because no time-varying surface elevation data was available. It can be reasonably expected that the surface elevation and shape changes during the modelled period. Adding a time-dependent surface profile would therefore increase the reliability of the results of the LPFAM.

The spin-up done to obtain fitting initial conditions was arbitrarily chosen, based on the timescale the model does not feel the initial conditions anymore, and by letting the model run for that time with 1957 conditions. There a multiple alternatives: change the timescale and changing the year to constantly run gives already many options. Testing them all was outside the scope of this research, but using a different spin-up method might give a more accurate description of the water table in 1957. For example, now a sharp drop in water table height is modelled in 1957 and 1958, which might be accurate but it might also be a small shock because of the obtained initial conditions.

To determine the most fitting hydraulic conductivity distribution, observations of the water table depth were used. The water table depth resulted from among others a radargram, where the water surface needed to be hand-picked from a figure. Furthermore, there are large gaps in the data tracks of the snow scooter. This happened because the radar could not detect a water table, the radar could penetrate at a maximum to a depth of approximately 30 metres. The model in this research has a depth of approximately 50-55 metres (spatially variable, dependent on EBFM output), and therefore, points that were modelled to have a water table depth from 30 - 55 metres could not be tested to observations. Having data on water table depths between 30 and 55 metres could increase the reliability of the tuning process, and could be obtained from future field campaigns.

One step in the processing of the raw observations (a radargram) to the depth of the observed water table is to highlight the possible water table in the radargram by hand. This is an non-automatic process, and it is vulnerable to errors. Possible ways to solve this in further research is by using pressure sensors in the ice cap to determine the water table height, or by digging snowpits to verify the GPR data.

The depth-coordinates of the EBFM output changes slightly every time step. In this model, the discretization of the model grid is every time step adjusted according to the new depth of the EBFM model. By doing that, the water balance is artificially disrupted in between time-steps, which makes the volume and therefore residence time calculations less robust. As can be observed in Figure 4.7a and 4.7b, the mean depth of the model decreased over time, because of compaction in the EBFM, so the average volume per column decreased every time-step because of the changing discretization, so the calculated residence times are likely an underestimation. If the water reaches the surface, the water table is at that time-step being fixed to the surface to prevent the model from overflowing. This is done to ensure a usefull MODFLOW run, because model output cannot be trusted when the water table exceeds the surface elevation, but it alters the water balance as well, because is effectively taken away from the grid. To counter the water balance disruption from the changing depth, and to improve the credibility of the results of the LPFAM, further research could vertically extent the model to the bedrock below the Lomonosovfonna ice cap. The vertical extent of the LPFAM in this research was constraint by the vertical extent of the EBFM input data, being roughly 55 meters. It is however known that the Lomonosovfonna has a thickness of ±192 meters (see Marchenko et al. (2017a)), so this model does only cover roughly the top 25% of the total vertical extent of the ice cap.

7.2 Significance

This research presents a horizontal flow model of a perennial firn aquifer, treated as a groundwater system, which is a novelty in the existing literature. This study presents the evolution of the aquifer in the past and for two future scenarios, thereby contributing to the understanding of the response of this perennial firn aquifer to climate change. Furthermore, in this research, dynamic characteristics of the aquifer were assessed and calculated, such as flow speed and direction, and how these characteristics change as the climate changes. While water table evolution and hydraulic conductivity are of interest for glaciologists and climate researchers, dynamic characteristics might be interesting for microbiological research, to assess what kind of microbiological life can be present in firn aquifers.

The LPFAM requires discretization parameters, storage and recharge rates as main inputs. It can therefore be used on other sites with perennials firn aquifers as well, if there are firn conditions known. It would be interesting to see how the model performs on the PFA on the GrIS for example, or if it could predict PFA formation on Antarctica. MODFLOW 6 is designed to let the user choose what parts to use, therefore decreasing computation time and increasing model readability. This makes it possible to add processes to the LPFAM, if that is required or data is available for different study sites

8   CONCLUSION

In this research, a horizontal flow model of a perennial firn aquifer was developed using MOD-FLOW 6 and FloPy. The model was tuned to observations using the hydraulic conductivity distribution, and was then run with historical data (1957 - 2019) and with two future scenarios (2019 - 2060): RCP 4.5 and RCP 8.5. We found that the PFA existed in 1957, and likely before that. There is a distinct positive trend in the water table height visible in all scenarios. The water table reacts immediately to meltwater input, and it can, for sufficiently high meltwater peaks, take multiple years for the PFA to get back at the water table height it was before the peak. Water table heights in the future scenarios are found to be more sensitive than in the historical run. The water table reaches the surface around 2045 for RCP 8.5 and 2047 for RCP 4.5, and in 2060 around 60 % of the surface cells contain a water table that equals the surface elevation. Flow magnitude shows a positive trend, and is sensitive to the changing density. Residence times fluctuate strongly in the historical run, but decrease gradualy in both future scenarios. Future research could focus on modelling PFA-firn interactions, for example by creating a two-way coupling between the LPFAM and a firn model.

9 Acknowledgements

I want to give a massive thanks to both my supervisors, Ward van Pelt and Carleen Reijmer, for their support during this thesis. Not only did they provide me with necessary input and feedback, but they also knew when to 'pull on the brake' when I got to ambitious for the time given for the project. I enjoyed and appreciated the informal way of communicating and their approachability, either digitally because of the Covid-19 situation or live at the University.

I also wish to show my gratitude to Veijo Pohjola, Rickard Petterson and Ward van Pelt for inviting me to join the expedition to Svalbard, that was supposed to happen in April 2020, but was unfortunately cancelled due to the Covid-19 situation. I want to thank Veijo Pohjola for his interest in my work, and the opportunities he gave me to present my work. I want to thank Rickard Petterson for offering me a part-time job as teaching assistant at Uppsala University, that was unfortunately also postponed due to the Covid-19 situation, and also for providing me with a laptop when my own machine decided to break down. I also want to thank Veijo Pohjola and Ward van Pelt for offering me a job at Uppsala University to continue my research on the Lomonosovfonna PFA.

I furthermore wish to thank Fritjof Fagerlund for his help to shine light on the in's and out's of the magical hydrological wonderland. Without his help, I would probably still be struggling with hydrological definitions and their implementations in MODFLOW 6.

References

Bakker, M, Post, V, Langevin, C.D, Hughes, J.D, White, J.T, Starn, J.J, and Fienen, M.N. (2018). *FloPy v3.2.9: U.S. Geological Survey Software Release*. Tech. rep. US Geological Survey.

Bartelt, Perry and Lehning, Michael (2002). "A physical SNOWPACK model for the Swiss avalanche warning: Part I: numerical model". In: *Cold Regions Science and Technology* 35.3, pp. 123–145.

Batu, Vedat (1998). *Aquifer hydraulics: a comprehensive guide to hydrogeologic data analysis*. John Wiley & Sons.

Ben-Israel, Adi (1966). "A Newton-Raphson method for the solution of systems of equations". In: *Journal of Mathematical analysis and applications* 15.2, pp. 243–252.

Bilt, Willem van der, Bakke, Jostein, Smedsrud, Lars H, Sund, Monica, Schuler, Thomas, Westermann, Sebastian, Wong, Wai Kwok, Sandven, Stein, Simpson, Matthew James Ross, Skogen, Morten D, et al. (2019). "Climate in Svalbard 2100". In:

Bintanja, Richard and Andry, Olivier (2017). "Towards a rain-dominated Arctic". In: *Nature Climate Change* 7.4, pp. 263–267.

Boetius, Antje, Anesio, Alexandre M, Deming, Jody W, Mikucki, Jill A, and Rapp, Josephine Z (2015). "Microbial ecology of the cryosphere: sea ice and glacial habitats". In: *Nature Reviews Microbiology* 13.11, pp. 677–690.

Brennen, CE (2005). *Fundamentals of multiphase flow*. Cambridge university press.

Catania, Ginny A and Neumann, TA (2010). "Persistent englacial drainage features in the Greenland Ice Sheet". In: *Geophysical Research Letters* 37.2.

Christianson, Knut, Kohler, Jack, Alley, Richard B, Nuth, Christopher, and van Pelt, WJJ (2015). "Dynamic perennial firn aquifer on an Arctic glacier". In: *Geophysical Research Letters* 42.5, pp. 1418–1426.

Christner, Brent C, Lavender, Heather F, Davis, Christina L, Oliver, Erin E, Neuhaus, Sarah U, Myers, Krista F, Hagedorn, Birgit, Tulaczyk, Slawek M, Doran, Peter T, and Stone, William C (2018). "Microbial processes in the weathering crust aquifer of a temperate glacier". In: *The Cryosphere* 12.11, pp. 3653–3669.

Church, John A, Clark, Peter U, Cazenave, Anny, Gregory, Jonathan M, Jevrejeva, Svetlana, Levermann, Anders, Merrifield, Mark A, Milne, Glenn A, Nerem, R Steven, Nunn, Patrick D, et al. (2013). *Sea level change*. Tech. rep. PM Cambridge University Press.

Day, Jonathan J, Bamber, Jonathan L, Valdes, Paul J, and Kohler, Jack (2012). "The impact of a seasonally ice free Arctic Ocean on the temperature, precipitation and surface mass balance of Svalbard". In: *The Cryosphere* 6, pp. 35–50.

Divine, Dmitry V and Dick, Chad (2006). "Historical variability of sea ice edge position in the Nordic Seas". In: *Journal of Geophysical Research: Oceans* 111.C1.

Everett, A, Murray, T, Selmes, N, Rutt, IC, Luckman, A, James, TD, Clason, Caroline, O'Leary, M, Karunarathna, H, Moloney, V, et al. (2016). "Annual down-glacier drainage of lakes and water-filled crevasses at Helheim Glacier, southeast Greenland". In: *Journal of Geophysical Research: Earth Surface* 121.10, pp. 1819–1833.

Forster, RR, Box, Jason E, Van Den Broeke, Michiel R, Miège, Clément, Burgess, Evan W, Van Angelen, Jan H, Lenaerts, JTM, Koenig, Lora S, Paden, John, Lewis, C, et al. (2014). "Extensive liquid meltwater storage in firn within the Greenland ice sheet". In: *Nature Geoscience* 7.2, pp. 95–98.

Fountain, Andrew G (1989). "The storage of water in, and hydraulic characteristics of, the firn of South Cascade Glacier, Washington State, USA". In: *Annals of Glaciology* 13, pp. 69–75.

Fountain, Andrew G and Walder, Joseph S (1998). "Water flow through temperate glaciers". In: *Reviews of Geophysics* 36.3, pp. 299–328.

Gallet, JC, Björkman, M, Borstad, C, Hodson, A, Jacobi, HW, Larose, C, Luks, B, Spolaor, A, Urazgildeeva, A, and Zdanowicz, C (2019). *Snow research in Svalbard: current status and knowledge gaps*.

Hansen, Brage B, Isaksen, Ketil, Benestad, Rasmus E, Kohler, Jack, Pedersen, Åshild Ø, Loe, Leif E, Coulson, Stephen J, Larsen, Jan Otto, and Varpe, Øystein (2014). "Warmer and wetter

winters: characteristics and implications of an extreme weather event in the High Arctic". In: *Environmental Research Letters* 9.11, p. 114021.

Hanssen-Bauer, I and Førland, EJ (1998). "Long-term trends in precipitation and temperature in the Norwegian Arctic: can they be explained by changes in atmospheric circulation patterns?" In: *Climate Research* 10.2, pp. 143–153.

Hanssen-Bauer, I, Førland, EJ, Hisdal, H, Mayer, S, AB, Sandø, and Sorteberg, A (2019). "Climate in Svalbard 2100". In: *A knowledge base for climate adaptation.*

Hawrylak, Monika and Nilsson, Emma (2019). *Spatial and Temporal Variations in a Perennial Firn Aquifer on Lomonosovfonna, Svalbard.*

Hubbard, BP, Sharp, MJ, Willis, IC, Nielsen, MKt, and Smart, CC (1995). "Borehole water-level variations and the structure of the subglacial hydrological system of Haut Glacier d'Arolla, Valais, Switzerland". In: *Journal of Glaciology* 41.139, pp. 572–583.

Isaksson, E, Pohjola, V, Jauhiainen, T, Moore, J, Pinglot, JF, Vaikmäe, R, van de Wal, R, Hagen, JO, Ivask, J, Karlöf, L, et al. (2001). "An ice core record from Lomonsovfonna, Svalbard: viewing the isotopic, chemical and structural data from 1920-1997 in relation to instrumental records". In: *J. Glaciol* 47.157, pp. 335–345.

Kingslake, Jonathan, Ely, Jeremy C, Das, Indrani, and Bell, Robin E (2017). "Widespread movement of meltwater onto and across Antarctic ice shelves". In: *Nature* 544.7650, pp. 349–352.

Koenig, LS, Miège, Clément, Forster, Richard R, and Brucker, Ludovic (2014). "Initial in situ measurements of perennial meltwater storage in the Greenland firn aquifer". In: *Geophysical Research Letters* 41.1, pp. 81–85.

Kovacs, Austin, Gow, Anthony J, and Morey, Rexford M (1995). "The in-situ dielectric constant of polar firn revisited". In: *Cold Regions Science and Technology* 23.3, pp. 245–256.

Kuipers-Munneke, P, Ligtenberg, SRM, Suder, Eric A, and Van den Broeke, Michiel R (2015). "A model study of the response of dry and wet firn to climate change". In: *Annals of Glaciology* 56.70, pp. 1–8.

Kuipers-Munneke, P, M. Ligtenberg, SRM, Van den Broeke, MR, Van Angelen, JH, and Forster, RR (2014). "Explaining the presence of perennial liquid water bodies in the firn of the Greenland Ice Sheet". In: *Geophysical Research Letters* 41.2, pp. 476–483.

Langevin, Christian D, Hughes, Joseph D, Banta, Edward R, Niswonger, Richard G, Panday, Sorab, and Provost, Alden M (2017). *Documentation for the MODFLOW 6 groundwater flow model.* Tech. rep. US Geological Survey.

Larose, Catherine, Berger, Sibel, Ferrari, Christophe, Navarro, Elisabeth, Dommergue, Aurélien, Schneider, Dominique, and Vogel, Timothy M (2010). "Microbial sequences retrieved from environmental samples from seasonal Arctic snow and meltwater from Svalbard, Norway". In: *Extremophiles* 14.2, pp. 205–212.

Lenaerts, JTM, Lhermitte, S, D, Reinhard, Ligtenberg, SRM, Berger, S, Helm, V, Smeets, CJPP, Van Den Broeke, MR, Van De Berg, WJ, Van Meijgaard, E, et al. (2017). "Meltwater produced by wind–albedo interaction stored in an East Antarctic ice shelf". In: *Nature climate change* 7.1, pp. 58–62.

Lenaerts, JTM, Ligtenberg, SRM, Medley, Brooke, Van de Berg, Willem Jan, Konrad, Hannes, Nicolas, Julien P, Van Wessem, J Melchior, Trusel, Luke D, Mulvaney, Robert, Tuckwell, Rebecca J, et al. (2018). "Climate and surface mass balance of coastal West Antarctica resolved by regional climate modelling". In: *Annals of Glaciology* 59.76pt1, pp. 29–41.

Lewis, D, Kriz, George J, and Burgy, Robert H (1966). "Tracer dilution sampling technique to determine hydraulic conductivity of fractured rock". In: *Water Resources Research* 2.3, pp. 533–542.

Ligtenberg, SRM, Helsen, MM, and Van den Broeke, MR (2011). "An improved semi-empirical model for the densification of Antarctic firn". In: *The Cryosphere* 5, pp. 809–819.

Marchenko, Sergey, Cheng, Gong, Lötstedt, Per, Pohjola, Veijo, Pettersson, Rickard, van Pelt, WJJ, and Reijmer, CH (2019). "Thermal conductivity of firn at Lomonosovfonna, Svalbard, derived from subsurface temperature measurements". In: *Cryosphere* 13.7, pp. 1843–1859.

Marchenko, Sergey, Pohjola, Veijo, Pettersson, Rickard, van Pelt, WJJ, Vega, Carmen P, Machguth, Horst, Bøggild, Carl E, and Isaksson, Elisabeth (2017a). "A plot-scale study of

firn stratigraphy at Lomonosovfonna, Svalbard, using ice cores, borehole video and GPR surveys in 2012–14". In: *Journal of Glaciology* 63.237, pp. 67–78.

Marchenko, Sergey, van Pelt, WJJ, Claremar, Björn, Pohjola, Veijo, Pettersson, Rickard, Machguth, Horst, and Reijmer, CH (2017b). "Parameterizing deep water percolation improves subsurface temperature simulations by a multilayer firn model". In: *Frontiers in Earth Science* 5, p. 16.

Miller, OL, Solomon, D Kip, Miège, Clément, Koenig, Lora S, Forster, Richard R, Montgomery, Lynn N, Schmerr, Nicholas, Ligtenberg, SRM, Legchenko, Anatoly, and Brucker, Ludovic (2017). "Hydraulic conductivity of a firn aquifer in southeast Greenland". In: *Frontiers in Earth Science* 5, p. 38.

Miller, OL, Solomon, D Kip, Miège, Clément, Koenig, Lora, Forster, Richard, Schmerr, Nicholas, Ligtenberg, SRM, Legchenko, Anatoly, Voss, Clifford I, Montgomery, Lynn, et al. (2020). "Hydrology of a perennial firn aquifer in Southeast Greenland: an overview driven by field data". In: *Water Resources Research*, e2019WR026348.

NGWA (Apr. 6, 2020). *NGWA*. URL: https://www.ngwa.org/what-is-groundwater/About-groundwater/unconfined-or-water-table-aquifers (visited on 04/06/2020).

Nordli, Øyvind, Przybylak, Rajmund, Ogilvie, Astrid EJ, and Isaksen, Ketil (2014). "Long-term temperature trends and variability on Spitsbergen: the extended Svalbard Airport temperature series, 1898–2012". In: *Polar research* 33.1, p. 21349.

NPI (2014). *Terrengmodell Svalbard (S0 Terrengmodell)*. DOI: 10.21334/npolar.2014.dce53a47. URL: https://doi.org/10.21334/npolar.2014.dce53a47.

Oppenheimer, Michael, Glavovic, Bruce, Hinkel, Jochen, van de Wal, R, Magnan, Alexandre K, Abd-Elgawad, Amro, Cai, Rongshuo, Cifuentes-Jara, Miguel, Deconto, Robert M, Ghosh, Tuhin, et al. (2019). "Sea level rise and implications for low lying Islands, coasts and communities". In:

Osuch, Marzena and Wawrzyniak, Tomasz (2016). "Climate projections in the Hornsund area, Southern Spitsbergen". In: *Polish Polar Research*, pp. 379–402.

Parizek, Byron R and Alley, Richard B (2004). "Implications of increased Greenland surface melt under global-warming scenarios: ice-sheet simulations". In: *Quaternary Science Reviews* 23.9-10, pp. 1013–1027.

Peeters, Bart, Pedersen, Åshild Ønvik, Loe, Leif Egil, Isaksen, Ketil, Veiberg, Vebjørn, Stien, Audun, Kohler, Jack, Gallet, Jean-Charles, Aanes, Ronny, and Hansen, Brage Bremset (2019). "Spatiotemporal patterns of rain-on-snow and basal ice in high Arctic Svalbard: detection of a climate-cryosphere regime shift". In: *Environmental Research Letters* 14.1, p. 015002.

Pfeffer, W Tad, Box, Jason E, Fausto, Robert S, and Machguth, Horst (2018). *Melt Water Retention Processes in Snow and Firn on Ice Sheets and Glaciers: Observations and Modeling*. Frontiers Media SA.

Pohjola, V, Moore, JC, Isaksson, E, Jauhiainen, T, van de Wal, R, Martma, T, Meijer, HAJ, and Vaikmäe, R (2002). "Effect of periodic melting on geochemical and isotopic signals in an ice core from Lomonosovfonna, Svalbard". In: *Journal of Geophysical Research: Atmospheres* 107.D4, ACL–1.

Poinar, Kristin, Joughin, Ian, Lilien, David, Brucker, Ludovic, Kehrl, Laura, and Nowicki, Sophie (2017). "Drainage of Southeast Greenland firn aquifer water through crevasses to the bed". In: *Frontiers in Earth Science* 5, p. 5.

Reijmer, CH and Hock, Regine (2008). "Internal accumulation on Storglaciären, Sweden, in a multi-layer snow model coupled to a distributed energy- and mass-balance model". In: *Journal of Glaciology* 54.184, pp. 61–72. DOI: 10.3189/002214308784409161.

Ringrose, Philip and Bentley, Mark (2016). *Reservoir model design*. Springer.

Rodionov, Sergei N (2004). "A sequential algorithm for testing climate regime shifts". In: *Geophysical Research Letters* 31.9.

Schaap, Thomas, Roach, Michael J, Peters, Leo E, Cook, Sue, Kulessa, Bernd, and Schoof, Christian (2019). "Englacial drainage structures in an East Antarctic outlet glacier". In: *Journal of Glaciology*, pp. 1–9.

Serreze, Mark C and Barry, Roger G (2011). "Processes and impacts of Arctic amplification: A research synthesis". In: *Global and planetary change* 77.1-2, pp. 85–96.

Shannon, Sarah R, Payne, Antony J, Bartholomew, Ian D, Van Den Broeke, Michiel R, Edwards, Tamsin L, Fettweis, Xavier, Gagliardini, Olivier, Gillet-Chaulet, Fabien, Goelzer, Heiko, Hoffman, Matthew J, et al. (2013). "Enhanced basal lubrication and the contribution of the Greenland ice sheet to future sea-level rise". In: *Proceedings of the National Academy of Sciences* 110.35, pp. 14156–14161.

Steger, Christian R, Reijmer, CH, Van Den Broeke, Michiel R, Wever, Nander, Forster, Richard R, Koenig, Lora S, Kuipers-Munneke, Peter, Lehning, Michael, Lhermitte, Stef, Ligtenberg, SRM, et al. (2017). "Firn meltwater retention on the Greenland ice sheet: A model comparison". In: *Frontiers in earth science* 5, p. 3.

Stenborg, Thorsten (1973). *Some viewpoints on the internal drainage of glaciers.* na.

Stevens, Ian T, Irvine-Fynn, Tristram DL, Porter, Philip R, Cook, Joseph M, Edwards, Arwyn, Smart, Martin, Moorman, Brian J, Hodson, Andy J, and Mitchell, Andrew C (2018). "Near-surface hydraulic conductivity of northern hemisphere glaciers". In: *Hydrological Processes* 32.7, pp. 850–865.

Stolte, J, Freijer, JI, Bouten, W, Dirksen, C, Halbertsma, JM, Van Dam, JC, Van den Berg, JA, Veerman, GJ, and Wösten, JHM (1994). "Comparison of six methods to determine unsaturated soil hydraulic conductivity". In: *Soil Science Society of America Journal* 58.6, pp. 1596–1603.

Urumović, Kosta and Urumović Sr, Kosta (2016). "The referential grain size and effective porosity in the Kozeny–Carman model". In: *Hydrology and Earth System Sciences* 20.5, p. 1669.

van de Wal, R, Boot, W, Van den Broeke, MR, Smeets, CJPP, Reijmer, CH, Donker, JJA, and Oerlemans, J (2008). "Large and rapid melt-induced velocity changes in the ablation zone of the Greenland Ice Sheet". In: *science* 321.5885, pp. 111–113.

van Pelt, WJJ and Kohler, Jack (2015). "Modelling the long-term mass balance and firn evolution of glaciers around Kongsfjorden, Svalbard". In: *Journal of Glaciology* 61.228, pp. 731–744.

van Pelt, WJJ, Kohler, Jack, Liston, GE, Hagen, Jon Ove, Luks, Bartek, Reijmer, CH, and Pohjola, Veijo (2016a). "Multidecadal climate and seasonal snow conditions in Svalbard". In: *Journal of Geophysical Research: Earth Surface* 121.11, pp. 2100–2117.

van Pelt, WJJ, Oerlemans, J, Reijmer, CH, Pettersson, Rikard, Pohjola, Veijo, Isaksson, E, and Divine, D (2013). "An iterative inverse method to estimate basal topography and initialize ice flow models". In: *The Cryosphere* 7, pp. 987–1006.

van Pelt, WJJ, Oerlemans, Johannes, Reijmer, CH, Pohjola, V, Pettersson, Rickard, and Van Angelen, JH (2012). "Simulating melt, runoff and refreezing on Nordenskiöldbreen, Svalbard, using a coupled snow and energy balance model". In: *The Cryosphere* 6, pp. 641–659.

van Pelt, WJJ, Pettersson, Rickard, Pohjola, Veijo, Marchenko, Sergey, Claremar, Björn, and Oerlemans, Johannes (2014). "Inverse estimation of snow accumulation along a radar transect on Nordenskiöldbreen, Svalbard". In: *Journal of Geophysical Research: Earth Surface* 119.4, pp. 816–835.

van Pelt, WJJ, Pohjola, Veijo, Pettersson, Rickard, Ehwald, Lena E, Reijmer, CH, Boot, Wim, and Jakobs, Constantijn L (2018). "Dynamic response of a High Arctic glacier to melt and runoff variations". In: *Geophysical Research Letters* 45.10, pp. 4917–4926.

van Pelt, WJJ, Pohjola, Veijo, Pettersson, Rickard, Marchenko, Sergey, Kohler, Jack, Luks, Bartek, Hagen, Jon Ove, Schuler, Thomas, Dunse, Thorben, Noël, Brice, et al. (2019). "A long-term dataset of climatic mass balance, snow conditions, and runoff in Svalbard (1957–2018)". In: *The Cryosphere* 13, pp. 2259–2280.

van Pelt, WJJ, Pohjola, Veijo, and Reijmer, CH (2016b). "The changing impact of snow conditions and refreezing on the mass balance of an idealized Svalbard glacier". In: *Frontiers in Earth Science* 4, p. 102.

Van Vuuren, Detlef P, Edmonds, Jae, Kainuma, Mikiko, Riahi, Keywan, Thomson, Allison, Hibbard, Kathy, Hurtt, George C, Kram, Tom, Krey, Volker, Lamarque, Jean-Francois, et al. (2011). "The representative concentration pathways: an overview". In: *Climatic change* 109.1-2, p. 5.

Vega, Carmen P, Pohjola, Veijo, Beaudon, Emilie, Claremar, Björn, van Pelt, WJJ, Pettersson, Rickard, Isaksson, Elisabeth, Martma, Tõnu, Schwikowski, Margit, and Bøggild, Carl E (2016). "A synthetic ice core approach to estimate ion relocation in anice field site experiencing periodical melt: a case study onLomonosovfonna, Svalbard". In: *The Cryosphere* 10, pp. 961–976.

Vionnet, V, Brun, E, Morin, S, Boone, A, Faroux, S, Le Moigne, P, Martin, E, and Willemet, JM (2012). "The detailed snowpack scheme Crocus and its implementation in SURFEX v7. 2". In:

Wever, N, Fierz, C, Mitterer, C, Hirashima, H, and Lehning, M (2014). "Solving Richards Equation for snow improves snowpack meltwater runoff estimations in detailed multi-layer snowpack model". In: *The Cryosphere* 8.1, p. 257.

Ypma, Tjalling J (1995). "Historical development of the Newton–Raphson method". In: *SIAM review* 37.4, pp. 531–551.

Zandi, Iraj (2013). *Advances in Solid–Liquid Flow in Pipes and Its Application.* Elsevier.

Zwally, H Jay, Abdalati, Waleed, Herring, Tom, Larson, Kristine, Saba, Jack, and Steffen, Konrad (2002). "Surface melt-induced acceleration of Greenland ice-sheet flow". In: *Science* 297.5579, pp. 218–222.